

SUMMeR: Sub-Nyquist MIMO Radar

David Cohen , Deborah Cohen , *Student Member, IEEE*, Yonina C. Eldar , *Fellow, IEEE*,
and Alexander M. Haimovich , *Fellow, IEEE*

Abstract—Multiple-input multiple-output (MIMO) radar exhibits several advantages with respect to the traditional radar array systems in terms of flexibility and performance. However, MIMO radar poses new challenges for both hardware design and digital processing. In particular, achieving high azimuth resolution requires a large number of transmit and receive antennas. In addition, digital processing is performed on samples of the received signal, from each transmitter to each receiver, at its Nyquist rate, which can be prohibitively large when high resolution is needed. Overcoming the rate bottleneck, sub-Nyquist sampling methods have been proposed that break the link between radar signal bandwidth and sampling rate. In this paper, we extend these methods to MIMO configurations and propose a sub-Nyquist MIMO radar (SUMMeR) system that performs both time and spatial compression. We present a range-azimuth-Doppler recovery algorithm from sub-Nyquist samples obtained from a reduced number of transmitters and receivers, that exploits the sparsity of the recovered targets' parameters. This allows us to achieve reduction in the number of deployed antennas and the number of samples per receiver, without degrading the time and spatial resolutions. Simulations illustrate the detection performance of SUMMeR for different compression levels and shows that both time and spatial resolution are preserved, with respect to classic Nyquist MIMO configurations. We also examine the impact of design parameters, such as antennas' locations and carrier frequencies, on the detection performance, and provide guidelines for their choice.

Index Terms—MIMO radar, Compressed sensing.

I. INTRODUCTION

MULTIPLE input multiple output (MIMO) [1] radar, which presents significant potential for advancing state-of-the-art modern radar in terms of flexibility and performance, poses new theoretical and practical challenges. This radar architecture combines multiple antenna elements both at the transmitter and receiver where each transmitter radiates a different waveform. Two main MIMO radar architectures

are colocated MIMO [2] in which the elements are close to each other, and multistatic MIMO [3] where they are widely separated. In this work, we focus on colocated MIMO.

Colocated MIMO radar systems exploit the waveform diversity, based on mutual orthogonality of the transmitted signals [4]. This generates a virtual array induced by the phase differences between transmit and receive antennas. Such systems thus achieve higher resolution than their phased-array counterparts with the same number of elements and transmissions, contributing to MIMO's popularity. This increased performance comes at the price of higher complexity in the transmitters and receivers design. MIMO radar systems belong to the family of array radars, which allow to recover simultaneously the targets range, Doppler and azimuth. This three-dimensional recovery results in high digital processing complexity. One of the main challenges of MIMO radar is thus coping with complicated systems in terms of cost, high computational load and complex implementation.

Assuming a sparse target scene, where the ranges, Dopplers and azimuths lie on a predefined grid, the authors in [5], [6] investigate compressed sensing (CS) [7] recovery for MIMO architectures. CS reconstruction is traditionally proposed to reduce the number of measurements required for the recovery of a sparse signal in some domain. However, in the works above, this framework is not used to reduce the spatial or time complexity, namely the number of antennas and samples, but is rather focused on mathematical guarantees of CS recovery in the presence of noise. To that end, the authors use a dictionary that accounts for every combination of azimuth, range and Doppler frequency on the grid and the targets' parameters are recovered by matching the received signal with dictionary atoms. The processing efficiency is thus penalized by a very large dictionary that contains every parameter combination.

Several recent works have considered applying CS to MIMO radar to reduce the number of antennas or the number of samples per receiver without degrading resolution. The partial problem of azimuth recovery of targets all in the same range-Doppler bin is investigated in [8]. There, spatial compression is performed, where the number of antennas is reduced while preserving the azimuth resolution. Beamforming is applied on the time domain samples obtained from the thinned array at the Nyquist rate and the azimuths are recovered using CS techniques. In [9]–[12], a time compression approach is adopted where the Nyquist samples are compressed in each antenna before being forwarded to the central unit. While [9], [10] exploit sparsity and use CS recovery methods, [11], [12] apply matrix completion techniques to recover the missing samples, prior to azimuth-Doppler [11]

Manuscript received December 21, 2016; revised December 18, 2017; accepted April 14, 2018. Date of publication May 21, 2018; date of current version July 10, 2018. The associate editor coordinating the review of this manuscript and approving it for publication was Prof. Amir Asif. This work was supported by the European Union's Horizon 2020 research and innovation program under Grant 646804-ERC-COG-BNYQ, and in part by the Israel Science Foundation under Grant 335/14. The work of Deborah Cohen was supported by the Azrieli Fellowship from Azrieli Foundation. (*Corresponding author: Deborah Cohen.*)

David Cohen, Deborah Cohen, and Y. C. Eldar are with the Electrical Engineering Department, Technion, Haifa 3200003, Israel (e-mail: davidco@technion.ac.il; deborah.co88@gmail.com; yonina@ee.technion.ac.il).

A. M. Haimovich is with the Department of Electrical and Computer Engineering, New Jersey Institute of Technology, Newark, NJ 07102 USA (e-mail: haimovic@njit.edu).

Color versions of one or more of the figures in this paper are available online at <http://ieeexplore.ieee.org>.

Digital Object Identifier 10.1109/TSP.2018.2838541

or range-azimuth-Doppler [12] reconstruction. However, the authors do not address sampling and processing rate reduction since the compression is performed in the digital domain, after sampling, and the missing samples are reconstructed before recovering the target's parameters. In all the above works, the recovery is performed in the time domain on acquired or recovered Nyquist rate samples for each antenna.

To reduce the sampling rate while preserving the range resolution, the authors in [13] consider frequency domain recovery. Similar ideas have also been used in the context of ultrasound imaging [14], [15]. The work in [13] demonstrates low-rate range-Doppler recovery in the context of radar with a single antenna, including sub-Nyquist acquisition and low-rate digital processing. Low-rate data acquisition is based on the ideas of Xampling [16], [17], which consist of an ADC performing analog prefiltering of the signal before taking point-wise samples. Here, the samples are a sub-set of digitally transformed Fourier coefficients of the received signal, that contain the information needed to recover the desired signal parameters using CS algorithms [7]. A practical analog front-end implementing such a sampling scheme in the context of radar is presented in [18]. To recover the targets range-Doppler from the sub-Nyquist samples, the authors introduce Doppler focusing, which is a coherent superposition of time shifted and modulated pulses. For any Doppler frequency, the received signals from different pulses are combined so that targets with corresponding Doppler frequencies come together in phase. This method improves the signal to noise ratio (SNR) by a factor of the number of pulses.

The work of [13] exploits the Xampling framework to break the link between radar signal bandwidth and sampling rate, which defines the time or range resolution. Here, we present the sub-Nyquist MIMO radar (SUMMeR) system, that extends this concept in the context of MIMO radar to break the link between the aperture and the number of antennas, which defines the spatial or azimuth resolution. We consider azimuth-range-Doppler recovery and apply the concept of Xampling both in space (antennas deployment) and in time (sampling scheme) in order to simultaneously reduce the required number of antennas and samples per receiver, without degrading the time and spatial resolution. In particular, we perform spatial and time compression while keeping the same resolution induced by Nyquist rate samples obtained from a full virtual array with low computational cost.

To this end, we express the "Xamples", or compressed samples, both in time and space, in terms of the targets unknown parameters, namely range, azimuth and Doppler, and show how these can be recovered efficiently from the sub-Nyquist samples. We first focus on range-azimuth recovery and then extend our approach to range-azimuth-Doppler. In both cases, we present necessary conditions on the minimal number of samples and antennas for perfect recovery in noiseless settings. We then derive reconstruction algorithms by extending the orthogonal matching pursuit (OMP) algorithm [7] to simultaneous sparse matrix recovery in order to solve a system of CS matrix equations. Finally, we show how our SUMMeR system can be enhanced so that the spatial compression does not reduce detection perfor-

mance, while increasing the maximum unambiguous Doppler. To do so, we utilize the free frequency bands resulting from spatial compression for additional transmissions, thus forming a virtual pulse repetition frequency (PRF).

Our approach is advantageous even in the traditional Nyquist regime both in time and space. In MIMO radar, two of the most popular techniques to ensure waveform orthogonality are code division multiple access (CDMA) and frequency division multiple access (FDMA), where CDMA is typically preferred. This is due to two essential drawbacks of FDMA: range-azimuth coupling [19]–[21] and limited range resolution to a single waveform's bandwidth [22], [23]. In this work, we adopt the FDMA framework and show that our processing overcomes these two drawbacks. This approach, in contrast to CDMA, allows to legitimately assume narrowband waveforms, which is key to azimuth resolution thus reconciling the trade-off between azimuth and range resolution. This topic is addressed in more detail in [24].

The main contributions of SUMMeR are as follows:

- 1) **Low rate sampling and digital processing** - the unknown target parameters are recovered from sub-Nyquist samples obtained using Xampling. Both sampling and digital processing are performed at a low rate.
- 2) **Reduced number of antennas** - beamforming is performed on the Xamples obtained from a reduced number of transmit and receive antennas while keeping a fixed aperture.
- 3) **Scaling with problem size** - we separate the three dimensions (range, azimuth and Doppler) by adapting OMP to matrix form, with several matrix system equations. This avoids the use of a large CS dictionary, where each column corresponds to a range-azimuth-Doppler hypothesis.
- 4) **Maximal bandwidth exploitation** - the enhanced version of SUMMeR exploits the frequency bands left vacant by spatial compression for additional transmissions, with improved maximum unambiguous Doppler while preserving the total bandwidth.
- 5) **Enhanced range-azimuth resolution capabilities** - FDMA waveforms simultaneously allow for narrowband single transmissions for high azimuth resolution and large total bandwidth to achieve high range resolution.

Our simulation results illustrate range-azimuth-Doppler recovery from low rate samples. In particular, we compare the detection performance of SUMMeR for different time and spatial compression levels with classic MIMO processing of Nyquist samples acquired on a full virtual array. We demonstrate that, under no compression, our FDMA processing achieves the detection performance of classic CDMA, even when wideband effects are neglected for the latter, giving it an advantage. We then demonstrate that our enhanced version of SUMMeR gains back the performance lost due to spatial compression. We further investigate the impact of several design parameters such as antennas' locations and transmissions' carrier frequencies on the detection performance and provide guidelines for their selection. Finally, we propose a heuristic grid refinement method that allows to cope with the case where the grid assumption on the delays, azimuths and Doppler frequencies, required in CS techniques, is not valid.

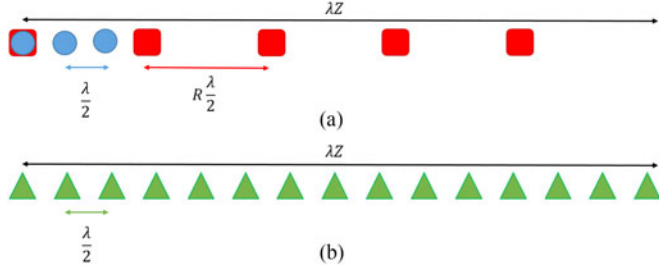


Fig. 1. Illustration of MIMO arrays. (a) Standard array. (b) Corresponding receiver virtual array.

This paper is organized as follows. In Section II, we review classic MIMO pulse-Doppler radar systems and processing. The SUMMeR system is described in Section III. Section IV introduces our sub-Nyquist sampling scheme and azimuth-range recovery algorithm, extended to range-azimuth-Doppler recovery in Section V. Numerical experiments are presented in Section VI.

II. CLASSIC MIMO RADAR

We begin by describing the classic MIMO radar architecture, in terms of array structure and waveforms, and the corresponding processing.

A. MIMO Architecture

The traditional approach to collocated MIMO adopts a virtual ULA structure [25], where R receivers, spaced by $\frac{\lambda}{2}$ and T transmitters, spaced by $R\frac{\lambda}{2}$ (or vice versa), form two ULAs. Here, λ is the signal wavelength. Coherent processing of the resulting TR channels generates a virtual array equivalent to a phased array with $TR\frac{\lambda}{2}$ -spaced receivers and normalized aperture $Z = \frac{TR}{2}$. This standard array structure and the corresponding virtual array are illustrated in Fig. 1 for $R = 3$ and $T = 5$. The blue circles represent the receivers and the red squares are the transmitters.

Each transmitting antenna sends P pulses, such that the m th transmitted signal is given by

$$s_m(t) = \sum_{p=0}^{P-1} h_m(t - p\tau) e^{j2\pi f_c t}, \quad 0 \leq t \leq P\tau, \quad (1)$$

where $h_m(t)$, $0 \leq m \leq T - 1$ are narrowband and orthogonal pulses with bandwidth B_h , modulated with carrier frequency f_c . The coherent processing interval (CPI) is equal to $P\tau$, where τ denotes the pulse repetition interval (PRI). For convenience, we assume that $f_c\tau$ is an integer, so that the delay $e^{-j2\pi f_c\tau p}$ is canceled in the modulation for $0 \leq p \leq P - 1$ [26]. The pulse time support is denoted by T_p , with $0 < T_p < \tau$.

MIMO radar architectures impose several requirements on the transmitted waveform family. Besides traditional demands from radar waveforms such as low sidelobes, MIMO transmit antennas rely on orthogonal waveforms. In addition, to avoid cross talk between the T signals and form TR channels, the orthogonality condition should be invariant to time shifts, that is $\int_{-\infty}^{\infty} s_i(t) s_j^*(t - \tau_0) dt = \delta(i - j)$, for $i, j \in [0, T - 1]$ and for

all τ_0 . This property implies that the orthogonal signals cannot overlap in frequency [27], leading to FDMA. Alternatively, time invariant orthogonality can be approximately achieved using CDMA.

Both FDMA and CDMA follow the general model [28]:

$$h_m(t) = \sum_{u=1}^{N_c} w_{mu} e^{j2\pi f_{mu} t} v(t - u\delta_t), \quad (2)$$

where each pulse is decomposed into N_c time slots with duration δ_t . Here, $v(t)$ denotes the elementary waveform, w_{mu} represents the code and f_{mu} the frequency for the m th transmission and u th time slot. The general expression (2) allows to analyze at the same time different waveform families. In particular, in CDMA, orthogonality is achieved by the code $\{w_{mu}\}_{u=1}^{N_c}$ and $f_{mu} = 0$ for all $1 \leq u \leq N_c$. In FDMA, $N_c = 1$, $w_{mu} = 1$ and $\delta_t = 0$. The center frequencies $f_{mu} = f_m$ are chosen in $[-\frac{TB_h}{2}, \frac{TB_h}{2}]$ so that the intervals $[f_m - \frac{B_h}{2}, f_m + \frac{B_h}{2}]$ do not overlap. For simplicity of notation, $\{h_m(t)\}_{m=0}^{T-1}$ can be considered as frequency-shifted versions of a low-pass pulse $v(t) = h_0(t)$ whose Fourier transform $H_0(\omega)$ has bandwidth B_h , such that

$$H_m(\omega) = H_0(\omega - 2\pi f_m). \quad (3)$$

We adopt a unified notation for the total bandwidth $B_{\text{tot}} = TB_h$ for FDMA and $B_{\text{tot}} = B_h$ for CDMA.

Consider L non-fluctuating point-targets, according to the Swerling-0 model [29]. It should be noted that the radar cross section (RCS) may vary with frequency for distributed targets. Unfortunately, when using coherent processing, the reflections from scatterers may interfere constructively or destructively depending on the signal frequency and the phases of the RCS for the individual scatterers [29], [30]. In this work, we adopt the point-target assumption and perform coherent processing. Extended targets can be modeled as the sum of point scatterers spread over the appropriate resolution bins [31].

Each target is identified by its parameters: RCS $\tilde{\alpha}_l$, distance between the target and the array origin or range R_l , velocity v_l and azimuth angle relative to the array θ_l . Our goal is to recover the targets' delay $\tau_l = \frac{2R_l}{c}$, azimuth sine $\vartheta_l = \sin(\theta_l)$ and Doppler shift $f_l^D = \frac{2v_l}{c} f_c$ from the received signals. In the sequel, the terms range and delay are used interchangeably, as well as azimuth angle and sine, and velocity and Doppler frequency, respectively.

B. Received Signal

The transmitted pulses are reflected by the targets and collected at the receive antennas. The following assumptions are adopted on the array structure and targets' location and motion, leading to a simplified expression for the received signal.

- A1** Collocated array - target RCS $\tilde{\alpha}_l$ and θ_l are constant over the array (see [32] for more details).
- A2** Far targets - target-radar distance is large compared to the distance change during the CPI, which allows for constant $\tilde{\alpha}_l$,

$$v_l P\tau \ll \frac{c\tau_l}{2}. \quad (4)$$

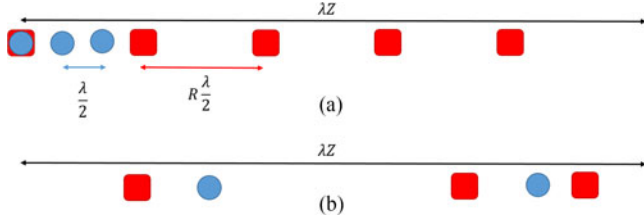


Fig. 3. Illustration of MIMO arrays. (a) Standard array. (b) Thinned array.

other hand, we propose to apply the Xampling framework [16] to both time (sampling scheme) and space (antennas deployment). Our goal can therefore be expressed more precisely as the estimation of the targets range, azimuth and velocities, i.e. τ_l , ϑ_l and f_l^D in (14), while reducing the number of samples, transmit and receive antennas.

In this work, we adopt the FDMA approach, in order to exploit the narrowband property of the transmitted waveforms. Classic FDMA presents two main drawbacks. First, due to the linear relationship between the carrier frequency and the index of antenna element, a strong range-azimuth coupling occurs [19]–[21]. The second drawback of FDMA is that the range resolution is limited to a single waveform’s bandwidth, namely B_h , rather than the overall transmit bandwidth $B_{\text{tot}} = TB_h$ [22], [23]. Here, we overcome these two drawbacks. First, to resolve the coupling issue, we randomly distribute the antennas, while keeping the carrier frequencies on a grid with spacing B_h . Second, by coherently processing the channels, we achieve a range resolution of $B_{\text{tot}} = TB_h$. This way, we exploit the overall received bandwidth that governs the range resolution, while maintaining the narrowband assumption for each channel, which is key to azimuth resolution. Our approach, presented in Sections IV and V, is applicable to both Nyquist and sub-Nyquist regimes, in time and space. Further discussion on FDMA versus CDMA in MIMO radar can be found in [24].

III. SUMMER SYSTEM MODEL

The SUMMER system implements compression in both space and time, reducing the number of antennas as well as the number of samples acquired by each receiver, while preserving range and azimuth resolution. We begin by describing spatial compression. Time compression is introduced in Section IV.

Consider a collocated MIMO radar system with $M < T$ transmit antennas and $Q < R$ receive antennas, whose locations are chosen uniformly at random within the aperture of the virtual array described above, that is $\{\xi_m\}_{m=0}^{M-1} \sim \mathcal{U}[0, Z]$ and $\{\zeta_q\}_{q=0}^{Q-1} \sim \mathcal{U}[0, Z]$, respectively. Note that, in principle, the antenna locations can be chosen on the ULAs’ grid. However, this configuration is less robust to range-azimuth ambiguity and leads to coupling between these parameters in the presence of noise, as shown in [24]. In Section IV, we derive lower bounds on the number of antennas M and Q . The spatially thinned array structure is illustrated in Fig. 3, for $Q = 2$ and $M = 3$.

Since we adopt a FDMA framework, spatial compression, which in particular reduces the number of transmit antennas, removes the corresponding transmitting frequency bands as well.

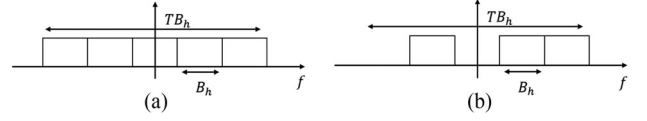


Fig. 4. FDMA transmissions. (a) Standard. (b) Spatial compression.

The transmitted signals are illustrated in Fig. 4 in the frequency domain. Fig. 4(a) and (b) show a standard FDMA transmission for $T = 5$ and the resulting signal after spatial compression for $M = 3$.

Our processing, described in Sections IV and V, allows to soften the strict neglect of the delay term in the transition from (12) to (13). We only remove $\eta_{m,q}\vartheta_l$ from the envelope $h_0(t)$, which stems from the array geometry. Then, (13) becomes

$$h_m(t - p\tau - \tau_l)e^{j2\pi f_m \eta_{m,q}\vartheta_l}. \quad (15)$$

Here, the restrictive assumption **A5** (8) is relaxed to $\frac{2Z\lambda}{c} \ll \frac{1}{B_h}$. We recall that in CDMA, (8) leads to a trade-off between azimuth and range resolution, by requiring either small aperture or small total bandwidth B_{tot} , respectively. Here, using the FDMA framework and less rigid approximation (15), we need only the single bandwidth B_h to be narrow, rather than the total bandwidth B_{tot} , eliminating the trade-off between range and azimuth resolution. The received signal at the q th antenna after demodulation to baseband is in turn given by

$$x_q(t) = \sum_{p=0}^{P-1} \sum_{m=0}^{M-1} \sum_{l=1}^L \alpha_l h_m(t - p\tau - \tau_l) e^{j2\pi\beta_{m,q}\vartheta_l} e^{-j2\pi f_l^D p\tau}, \quad (16)$$

where $\beta_{m,q} = (\zeta_q + \xi_m)(f_m \frac{\lambda}{c} + 1)$. It will be convenient to express $x_q(t)$ as a sum of single frames

$$x_q(t) = \sum_{p=0}^{P-1} x_q^p(t), \quad (17)$$

where

$$x_q^p(t) = \sum_{m=0}^{M-1} \sum_{l=1}^L \alpha_l h_m(t - \tau_l - p\tau) e^{j2\pi\beta_{m,q}\vartheta_l} e^{-j2\pi f_l^D p\tau}. \quad (18)$$

Our goal is to estimate the targets range, azimuth and velocity, i.e. to estimate τ_l , ϑ_l and f_l^D from low rate samples of $x_q(t)$, and a small number M and Q of antennas.

IV. SUB-NYQUIST RANGE-AZIMUTH RECOVERY

To introduce our sampling and processing, we begin by considering the special case of $P = 1$, namely a single pulse is transmitted by each transmit antenna. We first describe how the range-azimuth map can be recovered from Xamples in time and space. We then derive necessary conditions on the number of channels and samples per receiver to allow for perfect range-azimuth recovery in noiseless settings. Subsequently, in Section V, we treat the general case where a train of $P > 1$ pulses is transmitted by each antenna, and present a joint range-azimuth-Doppler recovery algorithm from Xamples, as well as recovery conditions.

A. Xampling in Time and Space

We begin by deriving an expression for the Fourier coefficients of the received signal, and show how the unknown parameters, namely τ_l and ϑ_l , are embodied in these coefficients. We then briefly explain how the Fourier coefficients may be obtained from low rate samples of the signal.

The received signal $x_q(t)$ at the q th antenna is limited to $t \in [0, \tau]$ and thus can be represented by its Fourier series

$$x_q(t) = \sum_{k \in Z} c_q[k] e^{j2\pi kt/\tau}, \quad t \in [0, \tau], \quad (19)$$

where, for $-\frac{NT}{2} \leq k \leq \frac{NT}{2} - 1$, with $N = \tau B_h$,

$$\begin{aligned} c_q[k] &= \frac{1}{\tau} \int_0^\tau x_q(t) e^{-j2\pi kt/\tau} dt \\ &= \frac{1}{\tau} \sum_{m=0}^{M-1} \sum_{l=1}^L \alpha_l e^{j2\pi\beta_{m,q}\vartheta_l} e^{-j\frac{2\pi}{\tau}k\tau_l} H_m \left(\frac{2\pi}{\tau}k \right). \end{aligned} \quad (20)$$

In order to obtain the Fourier coefficients $c_q[k]$ in (20) from low-rate samples of the received signal $x_q(t)$, we use the sub-Nyquist sampling scheme presented in [13], [18]. For each received transmission, Xampling allows one to obtain an arbitrary set κ , comprised of $K = |\kappa|$ frequency components from K point-wise samples of the received signal after appropriate analog preprocessing. Therefore, MK Fourier coefficients are acquired at each receiver from MK samples, with K coefficients per frequency band or transmission.

Once the Fourier coefficients $c_q[k]$, for $k \in \kappa$, are acquired, we separate them into channels for each transmitter, by exploiting the fact that they do not overlap in frequency. Applying a matched filter, we have

$$\begin{aligned} \tilde{c}_{q,m}[k] &= c_q[k] H_m^* \left(\frac{2\pi}{\tau}k \right) \\ &= \frac{1}{\tau} \left| H_m \left(\frac{2\pi}{\tau}k \right) \right|^2 \sum_{l=1}^L \alpha_l e^{j2\pi\beta_{m,q}\vartheta_l} e^{-j\frac{2\pi}{\tau}k\tau_l}. \end{aligned} \quad (21)$$

Let $y_{m,q}[k] = \frac{\tau}{|H_0(\frac{2\pi}{\tau}k)|^2} \tilde{c}_{q,m}[k + f_m\tau]$ be the normalized and aligned Fourier coefficients of the channel between the m th transmitter and q th receiver. Then,

$$y_{m,q}[k] = \sum_{l=1}^L \alpha_l e^{j2\pi\beta_{m,q}\vartheta_l} e^{-j\frac{2\pi}{\tau}k\tau_l} e^{-j2\pi f_m\tau_l}, \quad (22)$$

for $k \in \kappa$. Our goal is then to recover the targets' parameters τ_l and ϑ_l from $y_{m,q}[k]$.

B. Range-Azimuth Recovery Conditions

We now derive the minimal number of channels MQ and samples per receiver MK required for perfect range-azimuth recovery from (22) in a noiseless environment. Theorem 1 considers continuous settings while in Theorem 2, we assume that the delays and azimuths are confined to the Nyquist grid.

Theorem 1: *The minimal number of channels required for perfect recovery of L targets in noiseless settings is $MQ \geq 2L$ with a minimal number of $MK \geq 2L$ samples per receiver.*

Proof: Since there are no constraints on the delays or azimuths, let us examine the worst case where all targets have identical azimuth $\vartheta_l = \vartheta_0$. Equation (22) then becomes

$$y_{m,q}[k] = e^{j2\pi\beta_{m,q}\vartheta_0} \sum_{l=1}^L \alpha_l e^{-j\frac{2\pi}{\tau}(k+f_m\tau)\tau_l}. \quad (23)$$

For each channel, that is combination of the m th transmitter and q th receiver, we normalize (23) as $z_{m,q}[k] = y_{m,q}[k]/e^{j2\pi\beta_{m,q}\vartheta_0}$, yielding

$$z_{m,q}[k] = \sum_{l=1}^L \alpha_l e^{-j\frac{2\pi}{\tau}(k+f_m\tau)\tau_l}. \quad (24)$$

Since f_m are chosen so that the frequency intervals $[f_m - \frac{B_h}{2}, f_m + \frac{B_h}{2}]$ do not overlap, there are MK distinct values of $k + f_m\tau$, for $k \in \kappa$ and $0 \leq m \leq M - 1$. If it were possible to solve (24) with less than MK samples, then we could use this to solve the one-dimensional problem of $2L$ delay-amplitude recovery with less than $2L$ samples, in contradiction with [34]. Therefore, it holds that $MK \geq 2L$.

Consider now the worst case where all targets have the same delay $\tau_l = \tau_0$. We obtain

$$y_{m,q}[k] = e^{-j\frac{2\pi}{\tau}k\tau_0} e^{-j2\pi f_m\tau_0} \sum_{l=1}^L \alpha_l e^{j2\pi\beta_{m,q}\vartheta_l}, \quad (25)$$

and after normalization,

$$\tilde{z}_{m,q}[k] = \frac{1}{e^{-j\frac{2\pi}{\tau}(k+f_m\tau)\tau_0}} y_{m,q}[k] = \sum_{l=1}^L \alpha_l e^{j2\pi\beta_{m,q}\vartheta_l}. \quad (26)$$

Here, the number of distinct values of $\beta_{m,q}$ is at most MQ . The upper bound can be achieved by an appropriate choice of ξ_m and ζ_q , for $0 \leq m \leq M - 1$ and $0 \leq q \leq Q - 1$. Applying the same considerations, we infer that $MQ \geq 2L$. ■

As in traditional MIMO, suppose we now limit ourselves to the Nyquist grid with respect to the total bandwidth TB_h so that $\tau_l = \frac{\tau}{TN} s_l$, where s_l is an integer satisfying $0 \leq s_l \leq TN - 1$ and $\vartheta_l = -1 + \frac{2}{TR} r_l$, where r_l is an integer in the range $0 \leq r_l \leq TR - 1$. Let \mathbf{Y}^m be the $K \times Q$ matrix with q th column given by $y_{m,q}[k]$, $k \in \kappa$. We can then write \mathbf{Y}^m as

$$\mathbf{Y}^m = \mathbf{A}^m \mathbf{X} (\mathbf{B}^m)^T. \quad (27)$$

Here, \mathbf{A}^m denotes the $K \times TN$ matrix whose (k, n) th element is $e^{-j\frac{2\pi}{TN}\kappa_k n} e^{-j2\pi\frac{f_m}{B_h}\frac{n}{T}}$ with κ_k the k th element in κ , \mathbf{B}^m is the $Q \times TR$ matrix with (q, p) th element $e^{j2\pi\beta_{m,q}(-1 + \frac{2}{TR}p)}$. The matrix \mathbf{X} is a $TN \times TR$ sparse matrix that contains the values α_l at the L indices (s_l, r_l) . Our goal is to recover \mathbf{X} from the measurement matrices \mathbf{Y}^m , $0 \leq m \leq M - 1$. The time and spatial resolution induced by \mathbf{X} are $\frac{\tau}{TN} = \frac{1}{TB_h}$, and $\frac{2}{TR}$, respectively, as in classic CDMA processing.

Define

$$\mathbf{A} = [\mathbf{A}^{0T} \ \mathbf{A}^{1T} \ \dots \ \mathbf{A}^{(M-1)T}]^T, \quad (28)$$

and

$$\mathbf{B} = [\mathbf{B}^{0T} \ \mathbf{B}^{1T} \ \dots \ \mathbf{B}^{(M-1)T}]^T. \quad (29)$$

To better grasp the structure of \mathbf{A} and \mathbf{B} , consider the Nyquist regime, with carriers f_m lying on the grid $f_m = (m - \frac{T-1}{2})B_h$. In this case, the (k, n) th element of \mathbf{A}^m is $e^{-j\frac{2\pi}{TR}(k+mN-\frac{T-1}{2})n}$ and \mathbf{A} is the $TN \times TN$ Fourier matrix up to row permutation. Similarly, assuming that the antenna elements lie on the virtual array illustrated in Fig. 1, we have $\beta_{m,q} = \frac{1}{2}(q + mR)$, where we used $f_m \frac{\lambda}{c} \ll 1$ to simplify the expression. Then, the (q, p) th element of \mathbf{B}^m is $e^{j\frac{2\pi}{TR}(q+mR)(p-\frac{TR}{2})}$ and \mathbf{B} is the $TR \times TR$ Fourier matrix up to column permutation.

The matrices \mathbf{A} and \mathbf{B} are sometimes referred to as dictionaries, whose columns correspond to the range and azimuth grid points, respectively. Here, due to the reduction in the number of antennas and samples per receiver, the number of rows of \mathbf{A} and \mathbf{B} , namely MK and MQ , respectively, is decreased. In terms of samples, reducing the number of transmitters decreases the number of measurement matrices \mathbf{Y}^m , reducing the number of receivers removes the corresponding columns of all matrices \mathbf{Y}^m and reducing the number of samples per channel removes rows of \mathbf{Y}^m .

Theorem 2 presents necessary conditions on the minimal number of samples MK and number of channels MQ for perfect recovery of \mathbf{X} from (27) under the grid assumption.

Theorem 2: *The minimal number of channels required for perfect recovery of \mathbf{X} with L targets in noiseless settings is $MQ \geq 2L$ with a minimal number of $MK \geq 2L$ samples per receiver.*

We note that we obtain the same recovery conditions as in the continuous case of Theorem 1.

Proof: The observation model (27) for $0 \leq m \leq M-1$ can be equivalently written in vector form using the Kronecker product as

$$\text{vec}(\mathbf{Y}) \triangleq \begin{bmatrix} \text{vec}(\mathbf{Y}^0) \\ \text{vec}(\mathbf{Y}^1) \\ \vdots \\ \text{vec}(\mathbf{Y}^{M-1}) \end{bmatrix} = \begin{bmatrix} \mathbf{B}^0 \otimes \mathbf{A}^0 \\ \mathbf{B}^1 \otimes \mathbf{A}^1 \\ \vdots \\ \mathbf{B}^{M-1} \otimes \mathbf{A}^{M-1} \end{bmatrix} \text{vec}(\mathbf{X}). \quad (30)$$

Here $\text{vec}(\mathbf{X})$ is a column vector that vectorizes the matrix \mathbf{X} by stacking its columns and \otimes denotes the Kronecker product. It follows that $\text{vec}(\mathbf{X})$ is L -sparse. Denote

$$\mathbf{C} = \begin{bmatrix} \mathbf{B}^0 \otimes \mathbf{A}^0 \\ \mathbf{B}^1 \otimes \mathbf{A}^1 \\ \vdots \\ \mathbf{B}^{M-1} \otimes \mathbf{A}^{M-1} \end{bmatrix}. \quad (31)$$

In order to recover $\text{vec}(\mathbf{X})$ from $\text{vec}(\mathbf{Y})$, we require [7]

$$\text{spark}(\mathbf{C}) > 2L, \quad (32)$$

where $\text{spark}(\mathbf{C})$ is the smallest number of columns of \mathbf{C} that are linearly dependent [7], [17].

We now state the following lemma whose proof is presented in Appendix A.

Lemma 1: *Let $\mathbf{A}^m \in \mathbb{C}^{K,N}$ and $\mathbf{B}^m \in \mathbb{C}^{Q,R}$, for $0 \leq m \leq M-1$ with $K \leq N$ and $Q \leq R$. Denote $\mathbf{A} = [\mathbf{A}^{0T} \ \mathbf{A}^{1T} \ \dots$*

$\mathbf{A}^{(M-1)T}]^T$ and $\mathbf{B} = [\mathbf{B}^{0T} \ \mathbf{B}^{1T} \ \dots \ \mathbf{B}^{(M-1)T}]^T$. Then,

$$\text{spark}(\mathbf{C}) = \min\{\text{spark}(\mathbf{A}), \text{spark}(\mathbf{B})\}, \quad (33)$$

where \mathbf{C} is defined in (31).

From Lemma 1, (32) holds iff

$$\text{spark}(\mathbf{A}) > 2L \quad \text{and} \quad \text{spark}(\mathbf{B}) > 2L. \quad (34)$$

Here \mathbf{A} is of size $MK \times TN$ and \mathbf{B} is of size $MQ \times TR$. This in turn leads to both $MK \geq 2L$ and $MQ \geq 2L$. ■

Obviously, the design parameters $f_m, \xi_m, \zeta_q, |\kappa|$ should be chosen so that (34) is satisfied. In the simulations, these parameters are first chosen at random. Deterministic guidelines for their choice are then discussed in Section IV-D and in [24].

C. Range-Azimuth Recovery

To recover the sparse matrix \mathbf{X} from the set of equations (27), for all $0 \leq m \leq M-1$, where the targets' range and azimuth lie on the Nyquist grid, we would like to solve the following optimization problem

$$\min \|\mathbf{X}\|_0 \text{ s.t. } \mathbf{A}^m \mathbf{X} (\mathbf{B}^m)^T = \mathbf{Y}^m, \quad 0 \leq m \leq M-1. \quad (35)$$

To this end, we extend the matrix OMP from [35] to solve (35), as shown in Algorithm 1. In the algorithm description, $\text{vec}(\mathbf{Y})$ is defined in (30), $\mathbf{d}_t(l) = [(\mathbf{d}_t^0(l))^T \ \dots \ (\mathbf{d}_t^{M-1}(l))^T]^T$ where $\mathbf{d}_t^m(l) = \text{vec}(\mathbf{a}_{\Lambda_t(l,1)}^m (\mathbf{b}_{\Lambda_t(l,2)}^m)^T)$ with $\Lambda_t(l, i)$ the (l, i) th element in the index set Λ_t at the t th iteration, and $\mathbf{D}_t = [\mathbf{d}_t(1) \ \dots \ \mathbf{d}_t(t)]$. Here, \mathbf{a}_j^m denotes the j th column of the matrix \mathbf{A}^m and it follows that \mathbf{b}_j^m denotes the j th column of the matrix \mathbf{B}^m ; $\bar{\mathbf{B}}$ is the conjugate of \mathbf{B} . Once \mathbf{X} is recovered, the delays and azimuths are estimated as

$$\hat{\tau}_l = \frac{\tau}{TN} \Lambda_L(l, 1), \quad (36)$$

$$\hat{\theta}_l = -1 + \frac{2}{TR} \Lambda_L(l, 2). \quad (37)$$

Other CS recovery algorithms, such as FISTA [36]–[38], can also be extended to solve (35).

We conclude this subsection by briefly stating the main aspects in which our FDMA based processing differs from the classic CDMA approach introduced in Section II. A more extensive discussion can be found in [24]. First, the single spatial channel processing, which is equivalent to the matched filter in step (2), is limited to a range resolution of $1/B_h$ whereas in CDMA we achieve resolution of $1/B_{\text{tot}}$. In addition, in FDMA, the transmit steering vector is also range-dependent as a consequence of the frequency diversity, so that the range also depends on the channels, whereas in CDMA, it is decoupled from the channels domain. Therefore, our processing involves range-azimuth beamforming while the classic approach for CDMA uses beamforming on the azimuth domain only as in step (3). The range dependency on the channels in FDMA is exploited to enhance the poor range resolution of the single spatial channel $1/B_h$ to $1/TB_h = 1/B_{\text{tot}}$. These steps are summarized in Table I. Note that the processing is not divided into these two steps, which are provided for better understanding of the hidden connections in our problem. Specifically, the projection performed in step 2 of

TABLE I
JOINT RANGE-AZIMUTH FDMA PROCESSING

Processing Step	Governed By	Impact On
Single Spatial Channel	Fourier Coefficients (2nd term in (22))	Range Resolution: $1/B_h$ Unambiguous Range: τ
Range-Azimuth Beamforming (Over The Channels)	Carrier Frequencies (3rd term in (22))	Range Resolution: $1/TB_h$ Unambiguous Range: $1/B_h$
	Antenna Locations (1st term in (22))	Azimuth

Algorithm 1: SUMMeR for simultaneous sparse matrix recovery.

Input: Observation matrices \mathbf{Y}^m , measurement matrices \mathbf{A}^m , \mathbf{B}^m , for all $0 \leq m \leq M-1$

Output: Index set Λ containing the locations of the non zero indices of \mathbf{X} , estimate for sparse matrix $\hat{\mathbf{X}}$

1: Initialization: residual $\mathbf{R}_0^m = \mathbf{Y}^m$, index set $\Lambda_0 = \emptyset$, $t = 1$

2: Project residual onto measurement matrices:

$$\Psi = \mathbf{A}^H \mathbf{R} \bar{\mathbf{B}}$$

where \mathbf{A} and \mathbf{B} are defined in (28) and (29), respectively, and $\mathbf{R} = \text{diag}([\mathbf{R}_{t-1}^0 \cdots \mathbf{R}_{t-1}^{M-1}])$ is block diagonal

3: Find the two indices $\lambda_t = [\lambda_t(1) \ \lambda_t(2)]$ such that

$$[\lambda_t(1) \ \lambda_t(2)] = \arg \max_{i,j} |\Psi_{i,j}|$$

4: Augment index set $\Lambda_t = \Lambda_t \cup \{\lambda_t\}$

5: Find the new signal estimate

$$\hat{\alpha} = [\hat{\alpha}_1 \cdots \hat{\alpha}_t]^T = (\mathbf{D}_t^T \mathbf{D}_t)^{-1} \mathbf{D}_t^T \text{vec}(\mathbf{Y})$$

6: Compute new residual

$$\mathbf{R}_t^m = \mathbf{R}_0^m - \sum_{l=1}^t \alpha_l \mathbf{a}_{\Lambda_t(l,1)}^m (\mathbf{b}_{\Lambda_t(l,2)}^m)^T$$

7: If $t < L$, increment t and return to step 2, otherwise stop

8: Estimated support set $\hat{\Lambda} = \Lambda_L$

9: Estimated matrix $\hat{\mathbf{X}}$: $(\Lambda_L(l,1), \Lambda_L(l,2))$ -th component of $\hat{\mathbf{X}}$ is given by $\hat{\alpha}_l$ for $l = 1, \dots, L$ while rest of the elements are zero

the algorithm combines single spatial channel processing with range-azimuth beamforming.

D. Choice of Parameters

We now provide further insight into the choice of antennas' locations, Fourier coefficients and carrier frequencies which are embodied in (22) in the first, second and third terms,

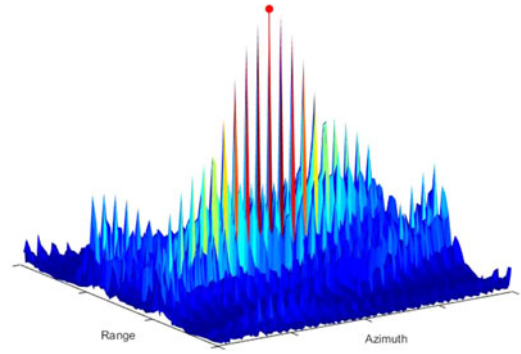


Fig. 5. Range-azimuth map in noiseless settings for antennas located on a conventional ULA and carrier frequencies selected on a grid, with $L = 1$ targets. The highest peak with the red circle corresponds to the true target. The other peaks result from range-azimuth coupling.

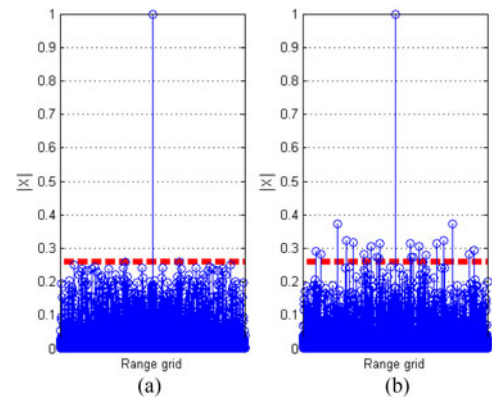


Fig. 6. Range-azimuth map in noiseless settings along range axis for choice of Fourier coefficients based on low coherence (left) and typical random choice (right), assuming $K = 50$, $M = Q = 20$ and $L = 1$. The red dotted line indicates the peak sidelobe level for this target in the range domain.

respectively. Then, we investigate the impact of these choices on the side lobes in the range and azimuth domains.

In [24], the impact of the joint choice of antennas location and carriers on range-azimuth coupling is explored. It is shown that under the ULA structure with transmit carriers on the grid, a strong range-azimuth coupling (Fig. 5) occurs. While the noiseless sufficient condition derived here in (32) still holds and the targets azimuth and range can be recovered, their detection in noisy conditions is impaired. As shown in [24], to overcome the ambiguity issue, either the antenna locations or the carrier frequencies, or both, should not lie on a specific grid. It was heuristically found that a configuration with random antennas' locations with carriers on a grid provides better results than random carriers with a ULA structure.

To minimize the sidelobe level in the range and azimuth domains, we define the matrices \mathbf{C}^1 , \mathbf{C}^2 , \mathbf{C}^3 corresponding to the first, second and third terms in (22) with respect to the Nyquist grid. The matrix \mathbf{C}^2 , which corresponds to the time domain (single spatial channel step in Table I), is a $K \times N$ matrix with each column corresponding to a range grid point discretized according to the poor range resolution of $1/B_h$ and large unambiguous

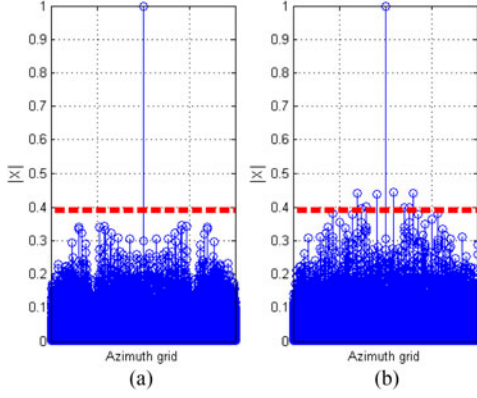


Fig. 7. Range-azimuth map in noiseless settings along range axis for choice of antennas' locations based on low coherence (left) and typical random choice (right), assuming $K = 50$, $M = Q = 20$ and $L = 1$. The red dotted line indicates the peak sidelobe level for this target in the range domain.

range τ , such that $C_{kn}^2 = e^{-j\frac{2\pi}{N}\kappa_k n}$. The matrices \mathbf{C}^1 and \mathbf{C}^3 are related to the channel domain (range-azimuth beamforming step in Table I). The columns of the $MQ \times TR$ matrix \mathbf{C}^1 correspond to azimuth grid points, so that $C_{ip}^1 = e^{j2\pi\beta_i(-1+\frac{2}{TR}p)}$, and \mathbf{C}^3 is a $MQ \times T$ matrix, whose columns correspond to range grid points discretized according to the higher range resolution $1/TB_h$ and small unambiguous range $1/B_h$, resulting in $C_{in}^3 = e^{-j2\pi\frac{f_i}{B_h}\frac{n}{T}}$. Since both \mathbf{C}^1 and \mathbf{C}^3 relate to the channel domain, we construct a combined matrix for range-azimuth beamforming in which each column corresponds to a pair of range-azimuth grid points which are resolved simultaneously. $\mathbf{C}^{13} = (\mathbf{1}^T \otimes \mathbf{C}^1) \odot (\mathbf{C}^3 \otimes \mathbf{1}^T)$, where \odot denotes the Hadamard product.

We consider the coherence defined as the maximum absolute value of cross-correlation between the columns of a matrix, namely

$$m^{(k)} = \max_{i \neq j} \left| (\mathbf{c}_i^k)^H \mathbf{c}_j^k \right|,$$

for $k = 2$ and $k = 13$. The design parameters are then chosen to minimize the coherence through trials of random selections. Specifically, the Fourier coefficients are chosen to minimize $m^{(2)}$ while the carrier frequencies and antennas' location are simultaneously selected to minimize $m^{(13)}$. Our criteria is particularly important when the time and/or spatial reduction factors are high since the sidelobes are slightly raised due to the small number of elements and time samples.

V. SUB-NYQUIST RANGE-AZIMUTH-DOPPLER RECOVERY

In Section IV, we introduced Xampling in time and space for range-azimuth recovery. We now return to our original range-azimuth-Doppler recovery problem. We begin by explaining how Xampling can be extended to the multi pulse signal (16). We then derive the minimal number of channels, samples per receiver and pulses per transmitter for perfect recovery in noiseless settings. Finally, we present our range-azimuth-Doppler recovery algorithm based on the concept of Doppler focusing introduced in [13].

Similarly to the derivations of Section IV, the p th frame of the received signal at the q th antenna, namely $x_q^p(t)$, is represented by its Fourier series

$$x_q^p(t) = \sum_{k \in \mathcal{Z}} c_q^p[k] e^{-j2\pi kt/\tau}, \quad t \in [p\tau, (p+1)\tau], \quad (38)$$

where, for $-\frac{NT}{2} \leq k \leq \frac{NT}{2} - 1$, with $N = \tau B_h$,

$$c_q^p[k] = \frac{1}{\tau} \sum_{m=0}^{M-1} \sum_{l=1}^L \alpha_l e^{j2\pi\beta_{m,q}\vartheta_l} e^{-j\frac{2\pi}{\tau}k\tau_l} e^{-j2\pi f_l^D p\tau} H_m\left(\frac{2\pi}{\tau}k\right). \quad (39)$$

After separation to channels by matched filtering, the normalized and aligned Fourier coefficients $y_{m,q}^p[k] = \frac{\tau}{H_0(\frac{2\pi}{\tau}k)^2} \tilde{c}_{q,m}^p[k + f_m\tau]$, with $\tilde{c}_{q,m}^p[k] = c_q^p[k] H_m^*\left(\frac{2\pi}{\tau}k\right)$, are given by

$$y_{m,q}^p[k] = \sum_{l=1}^L \alpha_l e^{j2\pi\beta_{m,q}\vartheta_l} e^{-j\frac{2\pi}{\tau}k\tau_l} e^{-j2\pi f_m\tau_l} e^{-j2\pi f_l^D p\tau}, \quad (40)$$

for $k \in \kappa$. The Fourier coefficients $y_{m,q}^p[k]$ of the frames of each channel (40) are identical to (22) except for the additional Doppler term $e^{-j2\pi f_l^D p\tau}$.

A. Range-Azimuth-Doppler Recovery Conditions

Theorems 3 and 4 below consider the minimal number of channels and samples per receiver required for perfect range-azimuth-Doppler recovery. Again, we consider both continuous and discrete settings, where in the latter, we assume that the delays, azimuths and Doppler frequencies lie on the Nyquist grid.

Theorem 3: *The minimal number of channels required for perfect recovery of L targets in noiseless settings is $MQ \geq 2L$ with a minimal number of $MK \geq 2L$ samples per receiver and $P \geq 2L$ pulses per transmitter.*

Proof: Repeating the proof of Theorem 1 for the worst cases where all targets have the same azimuth and Doppler frequency, we infer that $MK \geq 2L$. Similarly, the case where they all have the same delay and Doppler frequency yields $MQ \geq 2L$. Consider now the situation where all targets have the same delay $\tau_l = \tau_0$ and azimuth $\vartheta_l = \vartheta_0$, which constitutes a worst case as well. Then,

$$y_{m,q}^p[k] = e^{-j\frac{2\pi}{\tau_0}k\tau_0} e^{-j2\pi f_m\tau_0} e^{j2\pi\beta_{m,q}\vartheta_0} \sum_{l=1}^L \alpha_l e^{-j2\pi f_l^D p\tau}. \quad (41)$$

For each channel, we normalize (41) as

$$z_{m,q}^p[k] = \frac{y_{m,q}^p[k]}{e^{-j\frac{2\pi}{\tau_0}k\tau_0} e^{-j2\pi f_m\tau_0} e^{j2\pi\beta_{m,q}\vartheta_0}} = \sum_{l=1}^L \alpha_l e^{-j2\pi f_l^D p\tau}. \quad (42)$$

Applying the same considerations as in the proof of Theorem 1, we conclude that $P \geq 2L$. ■

As in Section IV, we next assume that the time delays, azimuths and Doppler frequencies are aligned to a grid. In particular, $\tau_l = \frac{\tau}{TN} s_l$, $\vartheta_l = -1 + \frac{2}{TR} r_l$ and $f_l^D = -\frac{1}{2\tau} + \frac{1}{P\tau} u_l$, where s_l , r_l and u_l are integers satisfying $0 \leq s_l \leq TN - 1$, $0 \leq r_l \leq TR - 1$ and $0 \leq u_l \leq P - 1$, respectively. Let \mathbf{Z}^m

be the $KQ \times P$ matrix with q th column given by the vertical concatenation of $y_{m,q}^p[k], k \in \kappa$, for $0 \leq q \leq Q - 1$. We can then write \mathbf{Z}^m as

$$\mathbf{Z}^m = (\mathbf{B}^m \otimes \mathbf{A}^m) \mathbf{X}_D \mathbf{F}^T. \quad (43)$$

Here, the $K \times TN$ matrix \mathbf{A}^m and the $Q \times TR$ matrix \mathbf{B}^m are defined in Section IV and \mathbf{F} denotes the $P \times P$ Fourier matrix up to column permutation. The matrix \mathbf{X}_D is a $T^2NR \times P$ sparse matrix that contains the values α_l at the L indices $(r_lTN + s_l, u_l)$.

Our goal now is to recover \mathbf{X}_D from the measurement matrices $\mathbf{Z}^m, 0 \leq m \leq M - 1$. The time, spatial and frequency resolution stipulated by \mathbf{X}_D are $\frac{1}{TB_h}$, $\frac{2}{TR}$ and $\frac{1}{P\tau}$ respectively. Theorem 4 presents necessary conditions on the minimal number of channels MQ , samples per receiver MK and pulses per transmitter P for perfect recovery of \mathbf{X}_D from (43) under the grid assumption.

Theorem 4: *The minimal number of channels required for perfect recovery of \mathbf{X}_D with L targets in noiseless settings is $MQ \geq 2L$ with a minimal number of $MK \geq 2L$ samples per receiver and $P \geq 2L$ pulses per transmitter.*

Proof: The observation model (43) can be equivalently written as

$$\mathbf{Z}^m \bar{\mathbf{F}} = P (\mathbf{B}^m \otimes \mathbf{A}^m) \mathbf{X}_D, \quad (44)$$

or in vector form,

$$\text{vec}(\mathbf{Z}\bar{\mathbf{F}}) \triangleq \begin{bmatrix} \text{vec}(\mathbf{Z}^0\bar{\mathbf{F}}) \\ \text{vec}(\mathbf{Z}^1\bar{\mathbf{F}}) \\ \vdots \\ \text{vec}(\mathbf{Z}^{M-1}\bar{\mathbf{F}}) \end{bmatrix} = P\mathbf{C}_D \text{vec}(\mathbf{X}_D), \quad (45)$$

where

$$\mathbf{C}_D = \begin{bmatrix} \mathbf{I}_P \otimes \mathbf{B}^0 \otimes \mathbf{A}^0 \\ \mathbf{I}_P \otimes \mathbf{B}^1 \otimes \mathbf{A}^1 \\ \vdots \\ \mathbf{I}_P \otimes \mathbf{B}^{M-1} \otimes \mathbf{A}^{M-1} \end{bmatrix}, \quad (46)$$

and \mathbf{I}_P denotes the $P \times P$ identity matrix. In order to recover the L -sparse vector $\text{vec}(\mathbf{X}_D)$ from $\text{vec}(\mathbf{Z})$, we require $\text{spark}(\mathbf{C}_D) > 2L$ [7].

Applying Lemma 1 twice, we obtain

$$\text{spark}(\mathbf{C}_D) = \min\{\text{spark}(\mathbf{A}), \text{spark}(\mathbf{B}), \text{spark}(\tilde{\mathbf{I}}_P)\}, \quad (47)$$

where $\tilde{\mathbf{I}}_P$ is the $MP \times P$ matrix which vertically concatenates M times the matrix \mathbf{I}_P . Obviously, $\text{spark}(\tilde{\mathbf{I}}_P) = \text{spark}(\mathbf{I}_P)$. Therefore, (32) holds iff

$$\text{spark}(\mathbf{A}) > 2L, \quad \text{spark}(\mathbf{B}) > 2L \quad \text{and} \quad \text{spark}(\mathbf{I}_P) > 2L, \quad (48)$$

which in turn leads to $MK \geq 2L$, $MQ \geq 2L$ and $P \geq 2L$. ■

From Theorems 2 and 4, the minimal number of channels to recover $2L$ targets is $MQ = 2L$. To minimize the total number of antennas $M + Q$, we choose $M, Q \in \mathbb{N}$, such that $\sqrt{2L} - 1 \leq M, Q \leq \sqrt{2L} + 1$ and $MQ \geq 2L$. The number of samples per channel must be at least $K \geq 2L/M$ with $P \geq 2L$ pulses. Obviously, these numbers are lower bounds and should be increased in the presence of noise.

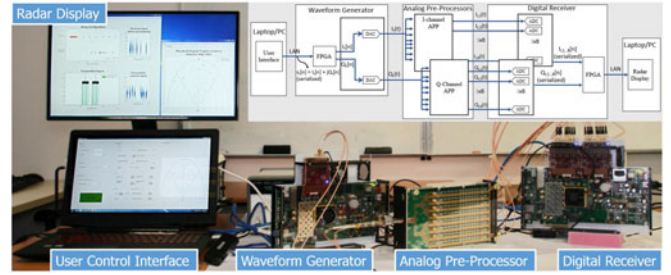


Fig. 8. FDMA MIMO prototype and user interface [41].

B. Range-Azimuth-Doppler Recovery

To recover jointly the range, azimuth and Doppler frequencies of the targets, we apply the concept of Doppler focusing from [13] to our setting. Once the Fourier coefficients (40) are acquired and processed, we perform Doppler focusing for a specific frequency ν , that is

$$\begin{aligned} \Phi_{m,q}^\nu[k] &= \sum_{p=0}^{P-1} y_{m,q}^p[k] e^{j2\pi\nu p\tau} \\ &= \sum_{l=1}^L \alpha_l e^{j2\pi\beta_{m,q}\vartheta_l} e^{-j\frac{2\pi}{\tau}(k+f_m\tau)\tau_l} \sum_{p=0}^{P-1} e^{j2\pi(\nu-f_l^D)p\tau}, \end{aligned} \quad (49)$$

for $k \in \kappa$. Following the same argument as in [13], it holds that

$$\sum_{p=0}^{P-1} e^{j2\pi(\nu-f_l^D)p\tau} \cong \begin{cases} P & |\nu - f_l^D| < \frac{1}{2P\tau}, \\ 0 & \text{otherwise.} \end{cases} \quad (50)$$

Therefore, for each focused frequency ν , (49) reduces to (22) and the resulting CS problem to solve is exactly (27), for $0 \leq m \leq M - 1$.

Doppler focusing performed on the Xamples is the frequency domain equivalent of classic Doppler processing involving the Doppler filter bank [33], performed in the time domain. Doppler focusing achieves a resolution of $1/P\tau$ following the classic property of the ambiguity function of a coherent train of pulses [39]. In addition, Doppler focusing increases the SNR by a factor of P , as can be seen in (50).

Algorithm 2 extends Algorithm 1 to solve (43) using Doppler focusing. Note that step 1 can be performed using the fast Fourier transform (FFT). In the algorithm description, $\text{vec}(\mathbf{Z})$ is defined similarly to $\text{vec}(\mathbf{Y})$ in (30), $\mathbf{e}_t(l) = [(\mathbf{e}_t^0(l))^T \cdots (\mathbf{e}_t^{M-1}(l))^T]^T$ where $\mathbf{e}_t^m(l) = \text{vec}((\mathbf{B}^m \otimes \mathbf{A}^m)_{\Lambda_t(l,2)TN+\Lambda_t(l,1)} (\mathbf{F}_{\Lambda_t(l,3)}^m)^T)$ with $\Lambda_t(l, i)$ the (l, i) th element in the index set Λ_t at the t th iteration, and $\mathbf{E}_t = [\mathbf{e}_t(1) \cdots \mathbf{e}_t(t)]$. Once \mathbf{X}_D is recovered, the delays and azimuths are given by (36) and (37), respectively and the Dopplers are estimated as

$$\hat{f}_l^D = -\frac{1}{2\tau} + \frac{1}{P\tau} \Lambda_L(l, 3). \quad (51)$$

Fig. 8 demonstrates a hardware prototype realizing the FDMA MIMO processing presented here. Further details can be found in [40] and [41].

Algorithm 2: SUMMeR for simultaneous sparse 3D recovery with focusing.

Input: Observation matrices \mathbf{Z}^m , measurement matrices \mathbf{A}^m , \mathbf{B}^m , for all $0 \leq m \leq M-1$

Output: Index set Λ containing the locations of the non zero indices of \mathbf{X}_D , estimate for sparse matrix $\hat{\mathbf{X}}_D$

1: Perform Doppler focusing for $0 \leq i \leq K-1$, $0 \leq j \leq Q-1$ and $0 \leq \nu \leq P-1$:

$$\Phi_{i,j}^{(m,\nu)} = (\mathbf{Z}^m \bar{\mathbf{F}})_{i+jK,\nu}$$

2: Initialization: residual $\mathbf{R}_0^{(m,\nu)} = \Phi^{(m,\nu)}$, index set $\Lambda_0 = \emptyset$, $t = 1$

3: Project residual onto measurement matrices for $0 \leq \nu \leq P-1$:

$$\Psi^\nu = \mathbf{A}^H \mathbf{R}^\nu \bar{\mathbf{B}},$$

where \mathbf{A} and \mathbf{B} are defined in (28) and (29), respectively, and $\mathbf{R}^\nu = \text{diag}([\mathbf{R}_{t-1}^{(0,\nu)} \dots \mathbf{R}_{t-1}^{(M-1,\nu)}])$ is block diagonal

1: Find the three indices $\lambda_t = [\lambda_t(1) \lambda_t(2) \lambda_t(3)]$ such that

$$[\lambda_t(1) \lambda_t(2) \lambda_t(3)] = \arg \max_{i,j,\nu} |\Psi_{i,j}^\nu|$$

5: Augment index set $\Lambda_t = \Lambda_{t-1} \cup \{\lambda_t\}$

6: Find the new signal estimate

$$\hat{\alpha} = [\hat{\alpha}_1 \dots \hat{\alpha}_t]^T = (\mathbf{E}_t^T \mathbf{E}_t)^{-1} \mathbf{E}_t^T \text{vec}(\mathbf{Z})$$

7: Compute new residual

$$\mathbf{R}_t^{(m,\nu)} = \mathbf{R}_0^{(m,\nu)} - \sum_{l=1}^t \alpha_l \mathbf{a}_{\Lambda_t(l,1)}^m (\mathbf{b}_{\Lambda_t(l,2)}^m)^T (\mathbf{f}_{\Lambda_t(l,3)})^T \mathbf{f}_\nu$$

8: If $t < L$, increment t and return to step 3, otherwise stop

9: Estimated support set $\hat{\Lambda} = \Lambda_L$

10: Estimated matrix $\hat{\mathbf{X}}_D$: the $(\Lambda_L(l,2)TN + \Lambda_L(l,1), \Lambda_L(l,3))$ -th component of $\hat{\mathbf{X}}_D$ is given by $\hat{\alpha}_l$ for $l = 1, \dots, L$ while the remaining elements are zero

C. Multi-Carrier SUMMeR

The frequency bands, within the total bandwidth, left vacant by the spatial compression can be exploited to increase the system's detection performance and unambiguous Doppler coverage without expanding the total bandwidth of $B_{\text{tot}} = TB_h$, thus preserving assumption **A3** (5). We refer to this approach as multi-carrier SUMMeR.

In multi-carrier SUMMeR the vacant frequency bands due to the spatial compression are utilized to add more pulses within the PRI as illustrated in Fig. 9. Denote by $\gamma = T/M$ the compression ratio of the number of transmitters. In multi-carrier SUMMeR, every transmit antenna sends γ pulses in each PRI. The pulses belong to different frequency bands and are therefore mutually orthogonal, such that the total number of user bands is $M\gamma B_h = TB_h$. The i th pulse of the p th PRI is transmitted at time $i\frac{T}{\gamma} + p\tau$, for $0 \leq i < \gamma$ and $0 \leq p \leq P-1$. The samples are then acquired and processed as described above. Besides increasing the detection performance as we show in simulations

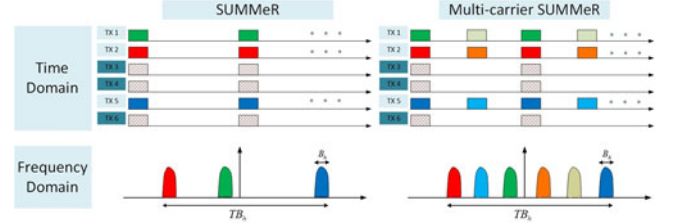


Fig. 9. In multi-carrier SUMMeR the free frequency bands are utilized for additional transmissions.

in Section VI, this method multiplies the unambiguous Doppler coverage by a factor of γ owing to the formed virtual PRF. Note, that the Doppler resolution is unchanged since the CPI, equal to $P\tau$, is unchanged. Keeping the CPI constant allows to preserve the stationary condition on the targets, that is assumptions **A2**, **A3** (5) and **A4** are still valid.

VI. SIMULATIONS

In this section, we present some numerical experiments illustrating both our range-azimuth and range-azimuth-Doppler recovery approaches. We compare our method with classic MIMO processing and examine the impact of the choice of several design parameters on the detection performance.

A. Preliminaries

Throughout the experiments, the standard MIMO system is based on a virtual array, as depicted in Fig. 3(a), which would be generated by $T = 20$ transmit antennas and $R = 20$ receive antennas, yielding an aperture $\lambda Z = 6$ m. The SUMMeR system is composed of $M < T$ transmitters and $Q < R$ receivers, with locations generated uniformly at random over the virtual array, as shown in Fig. 3(b). We use FDMA waveforms $h_m(t)$ such that $f_m = (i_m - \frac{T-1}{2})B_h$, where i_m are integers chosen uniformly at random in $[0, T)$, and with the following parameters: PRI $\tau = 100 \mu\text{sec}$, bandwidth $B_h = 5$ MHz and carrier $f_c = 10$ GHz. We consider targets from the Swerling-0 model with identical amplitudes and random phases. The received signals are corrupted with uncorrelated additive Gaussian noise (AWGN) with power spectral density N_0 . The SNR is defined as

$$\text{SNR} = \frac{\frac{1}{T_p} \int_0^{T_p} |h_0(t)|^2 dt}{N_0 B_h}. \quad (52)$$

We consider a hit-or-miss criterion as the performance metric. A “hit” is defined as a range-azimuth estimate which is identical to the true target position up to one Nyquist bin (grid point) defined as $1/TB_h$ and $2/TR$ for the range and azimuth, respectively. In pulse-Doppler settings, a “hit” is proclaimed if, in addition, the recovered Doppler is identical to the true frequency up to one Nyquist bin of size $1/P\tau$.

B. Numerical Results

1) *SUMMeR*: We first consider a sparse target scene with $L = 7$ targets including a couple of targets with close ranges

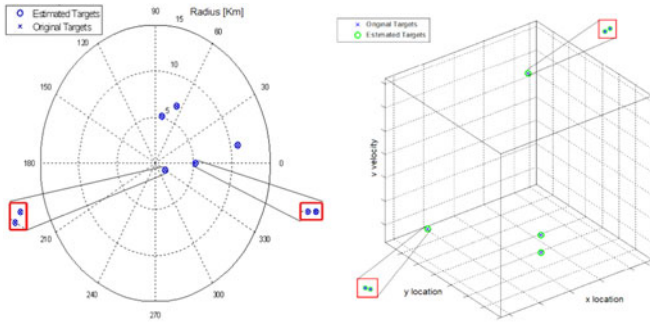


Fig. 10. Range-azimuth recovery for $L = 7$ targets and $\text{SNR} = 0$ dB (left), range-azimuth-Doppler recovery for $L = 6$ targets and $\text{SNR} = -10$ dB (right).

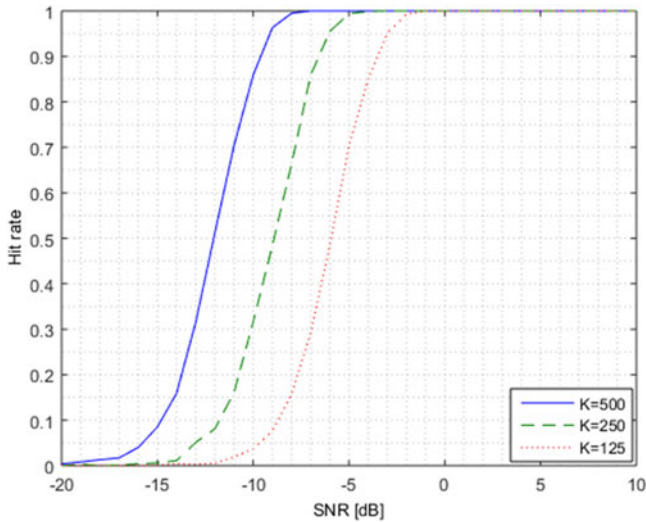


Fig. 11. Range-azimuth-Doppler recovery performance with time compression.

and another couple close in azimuth, both up to one grid point. We use $M = 10$ transmit antennas and $Q = 10$ receive antennas and employ $K = 250$ samples per channel instead of $N = B_h \tau = 500$, which corresponds to only 12.5% of the total number of Nyquist rate samples from the original array. The SNR is set to 0 dB. Fig. 10 (left pane) shows the sparse target scene on a range-azimuth map, where each real target is displayed with its estimated location. In the right pane, we demonstrate range-azimuth-Doppler recovery and show the location and velocity of $L = 6$ targets, including a couple of targets with close ranges, a couple with close azimuths and another couple with close velocities. Here, the range and azimuth are converted to 2-dimensional x and y locations. The SNR is set to -10 dB.

Next, we investigate the performance of our azimuth-range-Doppler recovery scheme with respect to SNR for different numbers of samples K per channel. We use the same array as described above, with spatial compression of 25%, where each transmitter sends $P = 10$ pulses. We consider $L = 10$ targets whose locations are generated uniformly at random. Each experiment is repeated over 100 realizations. Fig. 11 presents the range-azimuth-Doppler recovery performance with respect to

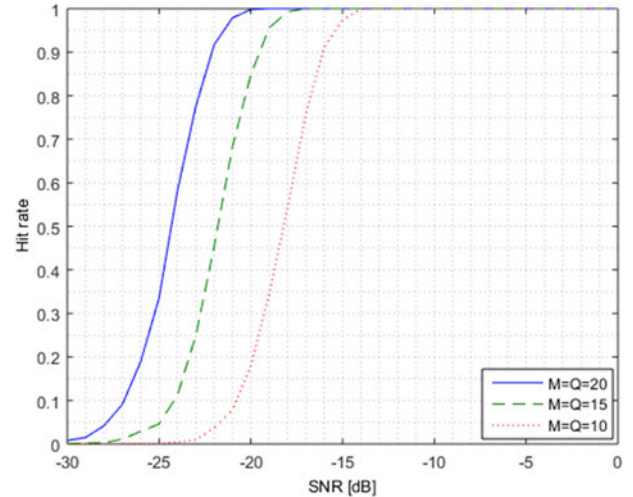


Fig. 12. Range-azimuth-Doppler recovery performance with spatial compression.

SNR. The configuration with $K = 500$ corresponds to samples obtained at the Nyquist rate. The configuration with $K = 125$ results in 1 : 4 time compression along with half the number of transmitters and receivers, yielding only 6.25% of the total number of Nyquist rate samples from the original array. From Fig. 11, it can be seen that the spatial compression yields a shift of 3 dB corresponding to half power reduction between successive graphs.

In Fig. 12 we consider the effect of spatial compression, using the configuration described above with fixed time compression of 50%, namely $K = 250$ samples per channel. We present the range-azimuth-Doppler recovery performance for different values of M and Q with respect to SNR. The configuration with $M = Q = 10$, yields a spatial compression of 25% with respect to the original array, and we indeed observe a 6 dB shift between the two graphs. For a system with fixed power the transmitting elements reduction will not affect the radiated energy which in turn leads to just a 3 dB SNR loss.

We further demonstrate the gain in SNR with increased number of pulses. We consider both spatial and time compression with $M = Q = 10$ and $K = 250$ and investigate two scenarios. In the first scenario, only $P = 1$ pulse is sent by each transmitter and we perform range-azimuth recovery. Here, a hit refers only to range-azimuth estimation. In the second scenario, each transmitter sends $P = 10$ pulses and we perform range-azimuth-Doppler recovery. In this setting, a hit refers to range-azimuth-Doppler estimation. Fig. 13 shows the hit rate for both scenarios. We clearly observe a 10 dB shift, corresponding to the SNR gain with $P = 10$ pulses in comparison with $P = 1$.

2) *Comparison of SUMMeR and Classic Processing:* We now compare our proposed range-azimuth recovery approach to the classic MIMO processing presented in Section II. For the classic method, we use bandlimited Gaussian pulses with bandwidth $B_h = 100$ MHz that are equivalent to the CDMA approach, and we neglect the wideband effects only for CDMA, giving it an advantage. Here, the SNR is defined with respect

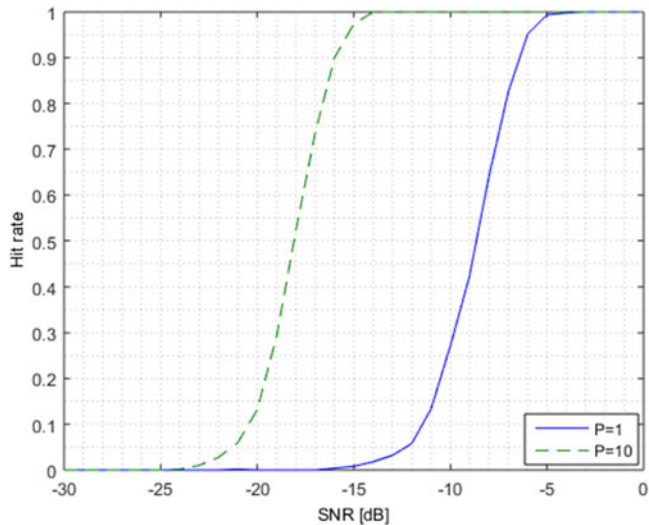


Fig. 13. SNR gain with number of pulses.

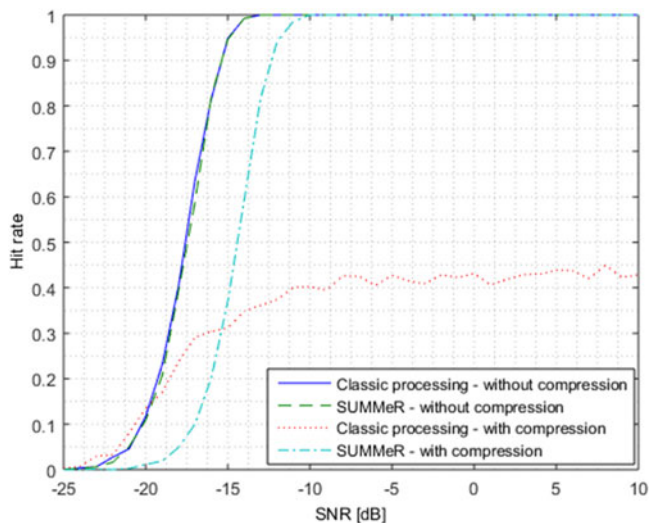


Fig. 14. Range-azimuth recovery performance of our proposed method vs. classic processing (spatial, or azimuth, resolution).

to the CDMA classic processing for the two methods to be comparable, namely

$$\text{SNR} = \frac{\frac{M}{T_p} \int_0^{T_p} |h_0(t)|^2 dt}{N_0 B_{\text{tot}}}. \quad (53)$$

In the first experiment, we consider $L = 2$ close targets in the spatial domain, up to one azimuth grid point. In each simulation, the pair of targets is generated at random. We consider two regimes: the first does not involve any compression, namely $M = T = 20$, $Q = R = 20$ and $K = N = 500$, while in the second, spatial compression is considered with $M = Q = 10$. Fig. 14 presents the range-azimuth recovery performance with respect to SNR for both approaches and both regimes.

In the second experiment, we choose $L = 2$ close targets in the time domain, namely up to one delay grid point. Again, we consider two regimes: the first with no compression and the second with time compression, specifically $K = 250$. In

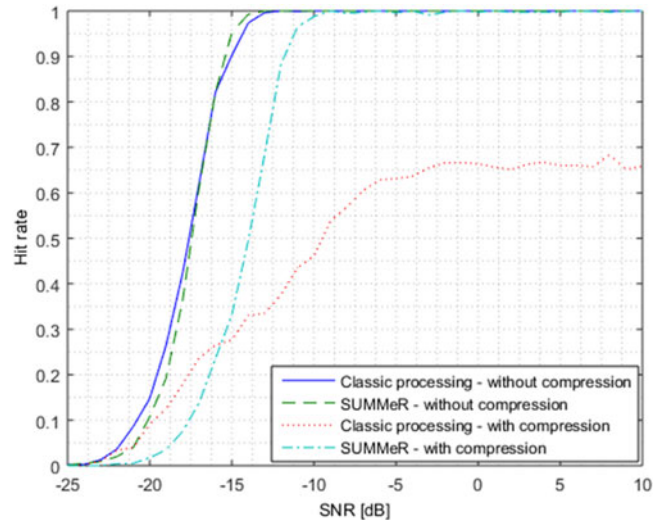


Fig. 15. Range-azimuth recovery performance of our proposed method vs. classic processing (time, or range, resolution).

our system, since the time resolution is determined by the total bandwidth, which depends on both transmitters and single bandwidth, we consider only $M = 10$ in the second regime for our method, while $M = T = 20$ for the classic approach. This way, we show that neither time nor spatial compression degrades the delay resolution. Fig. 15 presents the corresponding range-azimuth recovery performance.

We first observe that without compression both our FDMA approach and the conventional CDMA method are equivalent in terms of performance. Here, the wideband effects were neglected only for the classic CDMA method, which is thus given an advantage. In our settings, the delay $\eta_{mq} \vartheta_l$ due to the array geometry cannot be neglected, as in classic CDMA, since the array aperture $\lambda Z = 6$ m is only 4 times the range resolution $1/TB_h$ (1.25 m) so that (8) does not hold. Therefore, simulating wideband effects on the CDMA waveforms as well would further reduce the performance of conventional CDMA with respect to our proposed FDMA approach. In the case of 25% spatial compression in Fig. 14, the azimuth resolution of the classic approach is divided by 4, whereas the resolution of our approach remains unchanged. Therefore, even at high SNRs, two close targets in the spatial domain cannot be resolved since one can mask the other. Note that in low SNR, the classic processing seems to yield higher performance than ours. This stems from the fact that if the two close targets are in phase, then they can produce constructive signals and the classic approach will in fact detect the sum of both. A similar analysis may be carried out in the time domain with respect to the delay resolution in Fig. 15.

3) *Multi-Carrier SUMMeR*: We now illustrate the increased detection performance achieved by the multi-carrier SUMMeR method. We consider two regimes: the first does not involve any compression, while in the second, spatial compression is used with $M = Q = 10$. In the classic and SUMMeR system, $P = 10$ pulses are transmitted by each transmit antenna. In multi-carrier SUMMeR, we have $\gamma = 2$, leading to $2P = 20$

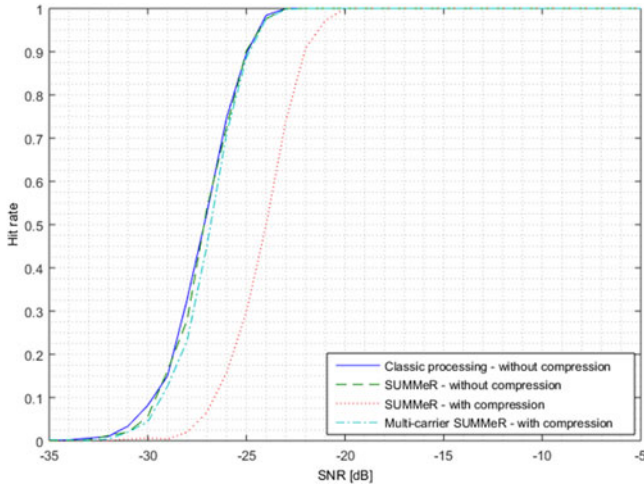


Fig. 16. Multi-carrier SUMMeR with spatial compression vs. classic processing and SUMMeR.

pulses per transmitter. For all configurations, we consider $L = 5$ targets. In Fig. 16, we observe that the multi-carrier approach with spatial compression achieves the same performance as the original SUMMeR and the classic processing with no compression. While using the SNR definition of (53), the number of transmitters does not affect the detection performance, since we have a system with fixed power. The reduction of the number of receivers decreases the performance by 3 dB, which is compensated for by the extra transmitted pulses. This shows that the same detection performance can be achieved by keeping the total transmission bandwidth while reducing the number of antennas. In fact, if the transmitters' reduction factor is greater than the receivers', then the detection performance of the multi-carrier SUMMeR system will be higher than that achieved by conventional processing without any compression.

4) *Off-Grid Targets*: Since in real scenarios, target delays and azimuths are not necessarily aligned to a grid, a finer grid can be used around detection points on the coarse grid to reduce quantization error. This technique, which we refer to as a dynamic grid, simply adds a step after support detection in each iteration (step 4 in Algorithm 1), that refines the grid around the detected azimuth, range and Doppler frequency. In particular, we define delay and azimuth matrices with respect to a fine grid over the detected range and azimuth bins and project the residual onto these matrices. The indices corresponding to the maximum of the new residual are then added to the support. In this experiment, we consider $L = 10$ off-grid targets with time and spatial compression. The accuracy performance improvement is illustrated in Figs. 17 and 18. Fig. 17 shows the maximal peak deviation $\rho = \max_l |\alpha_l - \hat{\alpha}_l|$, where the max is performed over the recovered targets. The dynamic grid step performed on off-grid targets allows to achieve the accuracy performance of targets on the grid which is also shown for reference. The remaining error results from mismodeling. Similarly, Fig. 18 presents the average range and azimuth deviations normalized to a resolution bin $\Delta R = 1/L \sum_{l=1}^L |r_l - \hat{r}_l|$ and $\Delta \theta = 1/L \sum_{l=1}^L |\theta_l - \hat{\theta}_l|$, respectively. Note that for both dynamic and static approaches,

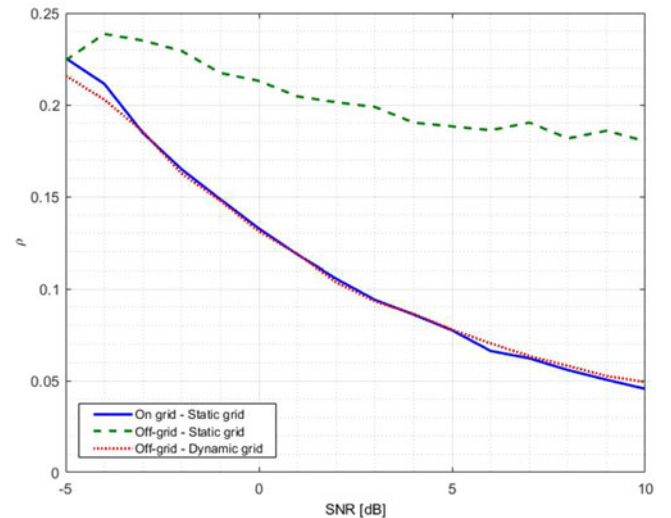


Fig. 17. Maximal peak deviation for $L = 10$ targets on the grid and off the grid, with and without the dynamic grid step, with time and spatial compression, $K = 250$, $M = Q = 10$.

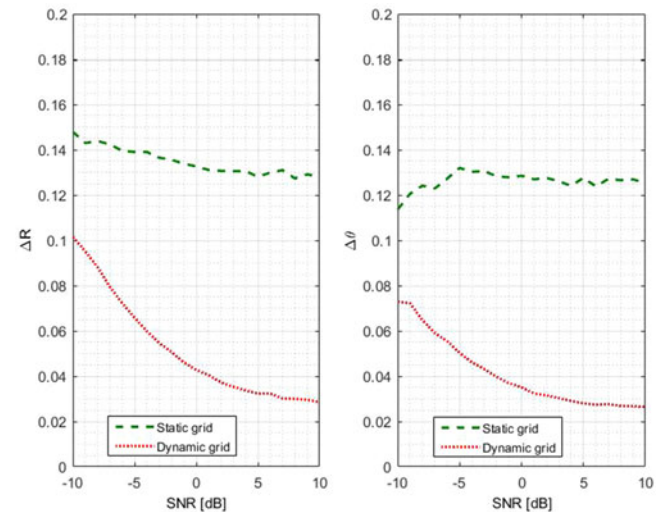


Fig. 18. Average range (left) and azimuth (right) deviation for $L = 10$ off grid targets, with and without the dynamic grid step, with time and spatial compression, $K = 250$, $M = Q = 10$.

the original grid is first expanded by a factor of 2 to alleviate the straddle loss effects [33]. The dynamic grid step can also be extended to range-azimuth-Doppler recovery.

VII. CONCLUSION

In this work, we presented the SUMMeR system, a sub-Nyquist MIMO radar sampling and recovery method, which exploits the concept of Xampling and Doppler focusing. This system breaks both the links between sampling rate and time resolution, and number of antennas and spatial resolution. We derived necessary conditions for range, azimuth and Doppler recovery, both with and without grid assumptions, that translate into minimal numbers of channels and samples per receiver for perfect recovery in noiseless settings. We next investigated the

impact of design parameters, such as antennas' locations, carrier frequencies and chosen Fourier coefficients, on the detection performance. While the CS approach adopted assumes that the targets parameters lie on a grid, we proposed a dynamic grid technique that allows to treat off-grid targets without decreasing the detection accuracy.

We compared our method with the classic Nyquist MIMO processing and showed that both the time and spatial resolution of our approach is preserved under time and spatial compression, in contrast to the traditional method. Furthermore, we proposed an enhanced version of SUMMeR, that exploits the frequency bands left vacant due to spatial compression, to recover the lost detection performance from this compression. Our processing provides a solution to FDMA's main drawbacks, range-azimuth coupling and range resolution limited to a single waveform's bandwidth, achieving the same performance as CDMA with enhanced range-azimuth resolution capabilities. Therefore, for high resolution applications our FDMA processing can outperform CDMA.

APPENDIX PROOF LEMMA 1

For convenience, we first repeat the lemma and then prove it.

Lemma 1: *Let $\mathbf{A}^m \in \mathbb{C}^{K,N}$ and $\mathbf{B}^m \in \mathbb{C}^{Q,R}$, for $0 \leq m \leq M-1$ with $K \leq N$ and $Q \leq R$. Denote $\mathbf{A} = [\mathbf{A}^{0^T} \ \mathbf{A}^{1^T} \ \dots \ \mathbf{A}^{(M-1)^T}]^T$ and $\mathbf{B} = [\mathbf{B}^{0^T} \ \mathbf{B}^{1^T} \ \dots \ \mathbf{B}^{(M-1)^T}]^T$. Let*

$$\mathbf{C} = \begin{bmatrix} \mathbf{B}^0 \otimes \mathbf{A}^0 \\ \mathbf{B}^1 \otimes \mathbf{A}^1 \\ \vdots \\ \mathbf{B}^{M-1} \otimes \mathbf{A}^{M-1} \end{bmatrix}. \quad (54)$$

Then,

$$\text{spark}(\mathbf{C}) = \min\{\text{spark}(\mathbf{A}), \text{spark}(\mathbf{B})\}. \quad (55)$$

Proof: The $MKQ \times NR$ matrix \mathbf{C} can be expressed more explicitly as

$$\mathbf{C} = \begin{bmatrix} b_{11}^0 \mathbf{A}^0 & \dots & b_{1R}^0 \mathbf{A}^0 \\ \vdots & \ddots & \vdots \\ b_{Q1}^0 \mathbf{A}^0 & \dots & b_{QR}^0 \mathbf{A}^0 \\ \vdots & \vdots & \vdots \\ b_{11}^{M-1} \mathbf{A}^{M-1} & \dots & b_{1R}^{M-1} \mathbf{A}^{M-1} \\ \vdots & \ddots & \vdots \\ b_{Q1}^{M-1} \mathbf{A}^{M-1} & \dots & b_{QR}^{M-1} \mathbf{A}^{M-1} \end{bmatrix}. \quad (56)$$

We first show that $\text{spark}(\mathbf{C}) \leq \min\{\text{spark}(\mathbf{A}), \text{spark}(\mathbf{B})\}$. By definition of $\text{spark}(\mathbf{A})$, there exists a vector $\mathbf{x}_A \in \mathbb{C}^N$ with $\|\mathbf{x}_A\|_0 = \text{spark}(\mathbf{A})$ such that $\mathbf{A}\mathbf{x}_A = \mathbf{0}$. Equivalently, $\mathbf{A}^m \mathbf{x}_A = \mathbf{0}$, for all $0 \leq m \leq M-1$. Let $\mathbf{y}_A = [\mathbf{x}_A^T \ 0 \ \dots \ 0]^T \in \mathbb{C}^{RN}$. Then, it holds that $\mathbf{C}\mathbf{y}_A = \mathbf{0}$ with $\|\mathbf{y}_A\|_0 = \|\mathbf{x}_A\|_0 = \text{spark}(\mathbf{A})$. Thus, $\text{spark}(\mathbf{C}) \leq \text{spark}(\mathbf{A})$.

We now use the fact that there exists permutation matrices $\mathbf{\Pi}_1$ and $\mathbf{\Pi}_2$ such that $\mathbf{B}^m \otimes \mathbf{A}^m = \mathbf{\Pi}_1 (\mathbf{A}^m \otimes \mathbf{B}^m) \mathbf{\Pi}_2$ [42], for all $0 \leq m \leq M-1$. By definition of $\text{spark}(\mathbf{B})$, there is a vector $\mathbf{x}_B \in \mathbb{C}^R$ with $\|\mathbf{x}_B\|_0 = \text{spark}(\mathbf{B})$ such that $\mathbf{B}\mathbf{x}_B = \mathbf{0}$.

Let $\tilde{\mathbf{y}}_B = [\mathbf{x}_B^T \ 0 \ \dots \ 0]^T \in \mathbb{C}^{NR}$ and $\mathbf{y}_B = \mathbf{\Pi}_2^{-1} \tilde{\mathbf{y}}_B$. Rewriting \mathbf{C} as

$$\mathbf{C} = \begin{bmatrix} \mathbf{\Pi}_1 (\mathbf{A}^0 \otimes \mathbf{B}^0) \mathbf{\Pi}_2 \\ \mathbf{\Pi}_1 (\mathbf{A}^1 \otimes \mathbf{B}^1) \mathbf{\Pi}_2 \\ \vdots \\ \mathbf{\Pi}_1 (\mathbf{A}^{M-1} \otimes \mathbf{B}^{M-1}) \mathbf{\Pi}_2 \end{bmatrix}, \quad (57)$$

we have $\mathbf{C}\mathbf{y}_B = \mathbf{0}$ with $\|\mathbf{y}_B\|_0 = \|\mathbf{x}_B\|_0 = \text{spark}(\mathbf{B})$. Therefore, $\text{spark}(\mathbf{C}) \leq \text{spark}(\mathbf{B})$.

We now show that $\text{spark}(\mathbf{C}) \geq \min\{\text{spark}(\mathbf{A}), \text{spark}(\mathbf{B})\}$. Assume first that $\text{spark}(\mathbf{A}) \geq \text{spark}(\mathbf{B})$. Then, we need to show that $\text{spark}(\mathbf{C}) \geq \text{spark}(\mathbf{B})$. Indeed, every column of \mathbf{C} has the form

$$\mathbf{c}_{w_j} = \begin{bmatrix} \mathbf{b}_{v_j}^0 \otimes \mathbf{a}_{u_j}^0 \\ \mathbf{b}_{v_j}^1 \otimes \mathbf{a}_{u_j}^1 \\ \vdots \\ \mathbf{b}_{v_j}^{M-1} \otimes \mathbf{a}_{u_j}^{M-1} \end{bmatrix}, \quad (58)$$

for $0 \leq w_j \leq NR-1$, $0 \leq u_j \leq N-1$, and $0 \leq v_j \leq R-1$. Suppose by contradiction that

$$\text{spark}(\mathbf{C}) = \ell < \text{spark}(\mathbf{B}). \quad (59)$$

In particular, this implies that any set of ℓ columns of \mathbf{B} is linearly independent, while there exist scalars $\lambda_1, \dots, \lambda_\ell$ not all 0 and indices u_1, \dots, u_ℓ and v_1, \dots, v_ℓ where $v_i \neq v_j$ for all $i \neq j$ such that

$$\sum_{j=1}^{\ell} \lambda_j \mathbf{c}_{w_j} = \sum_{j=1}^{\ell} \begin{bmatrix} (\lambda_j \mathbf{b}_{v_j}^0) \otimes \mathbf{a}_{u_j}^0 \\ (\lambda_j \mathbf{b}_{v_j}^1) \otimes \mathbf{a}_{u_j}^1 \\ \vdots \\ (\lambda_j \mathbf{b}_{v_j}^{M-1}) \otimes \mathbf{a}_{u_j}^{M-1} \end{bmatrix} = \mathbf{0}. \quad (60)$$

In (60), each index u_j can appear multiple times. Without loss of generality, we assume that the indices u_j are numbered in increasing order, so that

$$\underbrace{u_1 = \dots = u_{k_1}}_{g_1} < \dots < \underbrace{u_{k_{t-1}+1} = \dots = u_{k_t}}_{g_t}, \quad (61)$$

with $1 \leq t \leq \ell$. Therefore, we have

$$\sum_{i=1}^t \begin{bmatrix} \left(\sum_{j=k_{i-1}+1}^{k_i} \lambda_j \mathbf{b}_{v_j}^0 \right) \otimes \mathbf{a}_{g_i}^0 \\ \left(\sum_{j=k_{i-1}+1}^{k_i} \lambda_j \mathbf{b}_{v_j}^1 \right) \otimes \mathbf{a}_{g_i}^1 \\ \vdots \\ \left(\sum_{j=k_{i-1}+1}^{k_i} \lambda_j \mathbf{b}_{v_j}^{M-1} \right) \otimes \mathbf{a}_{g_i}^{M-1} \end{bmatrix} = \mathbf{0}, \quad (62)$$

where $k_0 = 0$ and $k_t = \ell$. Since $\text{spark}(\mathbf{A}) > \ell$, the vectors $\mathbf{a}_{g_1}, \dots, \mathbf{a}_{g_t}$ are linearly independent. It follows that

$$\sum_{j=k_{i-1}+1}^{k_i} \lambda_j \begin{bmatrix} \mathbf{b}_{v_j}^0 \\ \mathbf{b}_{v_j}^1 \\ \vdots \\ \mathbf{b}_{v_j}^{M-1} \end{bmatrix} = \mathbf{0}, \quad (63)$$

for $1 \leq i \leq t$. Since the sum in (63) is over at most ℓ columns of \mathbf{B} , this contradicts the assumption that $\text{spark}(\mathbf{B}) > \ell$.

Finally, assume $\text{spark}(\mathbf{B}) \geq \text{spark}(\mathbf{A})$. We then need to show that $\text{spark}(\mathbf{C}) \geq \text{spark}(\mathbf{A})$. This can be proved similarly to the previous case by writing the columns of \mathbf{C} as

$$\mathbf{c}_{w_j} = \begin{bmatrix} \mathbf{\Pi}_1 \left(\mathbf{b}_{v_j}^0 \otimes \mathbf{a}_{u_j}^0 \right) \\ \mathbf{\Pi}_1 \left(\mathbf{b}_{v_j}^1 \otimes \mathbf{a}_{u_j}^1 \right) \\ \vdots \\ \mathbf{\Pi}_1 \left(\mathbf{b}_{v_j}^{M-1} \otimes \mathbf{a}_{u_j}^{M-1} \right) \end{bmatrix}, \quad (64)$$

for $0 \leq w_j \leq NR - 1$, $0 \leq u_j \leq N - 1$, $0 \leq v_j \leq R - 1$ and where $\mathbf{\Pi}_1$ is an appropriate permutation matrix. ■

REFERENCES

- [1] E. Fishler, A. Haimovich, R. Blum, D. Chizhik, L. Cimini, and R. Valenzuela, "MIMO radar: An idea whose time has come," in *Proc. IEEE Radar Conf.*, 2004, pp. 71–78.
- [2] J. Li and P. Stoica, "MIMO radar with colocated antennas," *IEEE Signal Process. Mag.*, vol. 24, no. 5, pp. 106–114, Sep. 2007.
- [3] A. M. Haimovich, R. S. Blum, and L. J. Cimini, "MIMO radar with widely separated antennas," *IEEE Signal Process. Mag.*, vol. 25, no. 1, pp. 116–129, Jan. 2008.
- [4] J. Li and P. Stoica, *MIMO Radar Signal Processing*. New York, NY, USA: Wiley, 2009.
- [5] T. Strohmer and H. Wang, "Sparse MIMO radar with random sensor arrays and Kerdock codes," in *Proc. IEEE Int. Conf. Sampling Theory Appl.*, 2013, pp. 517–520.
- [6] T. Strohmer and B. Friedlander, "Analysis of sparse MIMO radar," *Appl. Comput. Harmonic Anal.*, vol. 37, pp. 361–388, 2014.
- [7] Y. C. Eldar and G. Kutyniok, *Compressed Sensing: Theory and Applications*. New York, NY, USA: Cambridge Univ. Press, 2012.
- [8] M. Rossi, A. M. Haimovich, and Y. C. Eldar, "Spatial compressive sensing for MIMO radar," *IEEE Trans. Signal Process.*, vol. 62, no. 2, pp. 419–430, Jan. 2014.
- [9] Y. Yu, A. P. Petropulu, and H. V. Poor, "MIMO radar using compressive sampling," *IEEE J. Sel. Topics Signal Process.*, vol. 4, no. 1, pp. 146–163, Feb. 2010.
- [10] M. H. Sajjadih and A. Asif, "Compressive sensing time reversal MIMO radar: Joint direction and doppler frequency estimation," *IEEE Signal Process. Lett.*, vol. 22, no. 9, pp. 1283–1287, Sep. 2015.
- [11] D. S. Kalogerias and A. P. Petropulu, "Matrix completion in colocated MIMO radar: Recoverability, bounds & theoretical guarantees," *IEEE Trans. Signal Process.*, vol. 62, no. 2, pp. 309–321, Jan. 2014.
- [12] S. Sun, W. U. Bajwa, and A. P. Petropulu, "MIMO-MC radar: A MIMO radar approach based on matrix completion," *IEEE Trans. Aerosp. Electron. Syst.*, vol. 51, no. 3, pp. 1839–1852, Jul. 2015.
- [13] O. Bar-Ilan and Y. C. Eldar, "Sub-Nyquist radar via Doppler focusing," *IEEE Trans. Signal Process.*, vol. 62, no. 7, pp. 1796–1811, Apr. 2014.
- [14] N. Wagner, Y. C. Eldar, and Z. Friedman, "Compressed beamforming in ultrasound imaging," *IEEE Trans. Signal Process.*, vol. 60, no. 9, pp. 4643–4657, Sep. 2012.
- [15] T. Chernyakova and Y. C. Eldar, "Fourier-domain beamforming: The path to compressed ultrasound imaging," *IEEE Trans. Ultrason., Ferroelect. Freq. Control*, vol. 61, no. 8, pp. 1252–1267, Aug. 2014.
- [16] M. Mishali, Y. C. Eldar, O. Dounaevsky, and E. Shoshan, "Xampling: Analog to digital at sub-Nyquist rates," *IET Circuits, Devices Syst.*, vol. 5, no. 1, pp. 8–20, 2011.
- [17] Y. C. Eldar, *Sampling Theory: Beyond Bandlimited Systems*. New York, NY, USA: Cambridge Univ. Press, 2015.
- [18] E. Baransky, G. Itzhak, I. Shmuel, N. Wagner, E. Shoshan, and Y. C. Eldar, "A sub-Nyquist radar prototype: Hardware and applications," *IEEE Trans. Aerosp. Electron. Syst.*, vol. 50, no. 2, pp. 809–822, Apr. 2014.
- [19] H. Sun, F. Brigui, and M. Lesturgie, "Analysis and comparison of MIMO radar waveforms," in *Proc. IEEE Int. Radar Conf.*, 2014, pp. 1–6.
- [20] M. Cattenoz, "MIMO radar processing methods for anticipating and preventing real world imperfections," Ph.D. dissertation, Signal and Image Processing, Université Paris Sud-Paris XI, Orsay, France, 2015.
- [21] O. Rabaste, L. Savy, M. Cattenoz, and J.-P. Guyvarch, "Signal waveforms and range/angle coupling in coherent colocated MIMO radar," in *Proc. IEEE Int. Conf. Radar*, 2013, pp. 157–162.
- [22] P. Vaidyanathan and P. Pal, "MIMO radar, SIMO radar, and IFIR radar: A comparison," in *Proc. Asilomar Conf. Signals, Syst. Comput.*, 2009, pp. 160–167.
- [23] J. P. Stralka, R. M. Thompson, J. Scanlan, and A. Jones, "MISO radar beamforming demonstration," in *Proc. IEEE RadarCon*, 2011, pp. 889–894.
- [24] D. Cohen, D. Cohen, and Y. C. Eldar, "High resolution FDMA MIMO radar," *CoRR*, vol. abs/1711.06560, 2017. [Online]. Available: <http://arxiv.org/abs/1711.06560>
- [25] C.-Y. Chen, "Signal processing algorithms for MIMO radar," Ph.D. dissertation, Electrical Engineering, California Inst. Technol., Pasadena, CA, USA, 2009.
- [26] P. Z. Peebles, *Radar Principles*. New York, NY, USA: Wiley, 2007.
- [27] P. Vaidyanathan, P. Pal, and C.-Y. Chen, "MIMO radar with broadband waveforms: Smearing filter banks and 2D virtual arrays," in *Proc. Asilomar Conf. Signals, Syst. Comput.*, 2008, pp. 188–192.
- [28] O. Rabaste, L. Savy, M. Cattenoz, and J.-P. Guyvarch, "Signal waveforms and range/angle coupling in coherent colocated MIMO radar," in *Proc. IEEE Int. Conf. Radar*, Sep. 2013, pp. 157–162.
- [29] M. Skolnik, *Radar Handbook*. New York, NY, USA: McGraw Hill, 1970.
- [30] F. Weinmann, "Frequency dependent RCS of a generic airborne target," in *Proc. URSI Int. Symp. Electrom. Theory*, 2010, pp. 977–980.
- [31] D. L. Mensa, "Wideband radar cross section diagnostic measurements," *IEEE Trans. Instrum. Meas.*, vol. 33, no. 3, pp. 206–214, Sep. 1984.
- [32] E. Fishler, A. Haimovich, R. S. Blum, and L. J. Cimini, "Spatial diversity in radars-models and detection performance," *IEEE Trans. Signal Process.*, vol. 54, no. 3, pp. 823–838, Mar. 2006.
- [33] M. A. Richards, *Fundamentals of Radar Signal Processing*. New York, NY, USA: McGraw-Hill, 2014.
- [34] M. Vetterli, P. Marziliano, and T. Blu, "Sampling signals with finite rate of innovation," *IEEE Trans. Signal Process.*, vol. 50, no. 6, pp. 1417–1428, Jun. 2002.
- [35] T. Wimalajeewa, Y. C. Eldar, and P. K. Varshney, "Recovery of sparse matrices via matrix sketching," *CoRR*, vol. abs/1311.2448, 2013. [Online]. Available: <http://arxiv.org/abs/1311.2448>
- [36] A. Beck and M. Teboulle, "A fast iterative shrinkage-thresholding algorithm for linear inverse problems," *SIAM J. Imag. Sci.*, vol. 2, pp. 183–202, 2009.
- [37] A. Yang, A. Ganesh, S. Sastry, and Y. Ma, "Fast ℓ_1 -minimization algorithms and an application in robust face recognition: A review," in *Proc. Int. Conf. Image Process.*, 2010, pp. 1849–1852.
- [38] D. P. Palomar and Y. C. Eldar, *Convex Optimization in Signal Processing and Communications*. New York, NY, USA: Cambridge Univ. Press, 2010.
- [39] N. Levanon and E. Mozeson, *Radar Signals*. New York, NY, USA: Wiley, 2004.
- [40] K. V. Mishra *et al.*, "Cognitive sub-Nyquist hardware prototype of a colocated MIMO radar," in *Proc. 4th Int. Workshop Compressed Sens. Theory Its Appl. Radar, Sonar Remote Sens.*, 2016, pp. 56–60.
- [41] D. Cohen *et al.*, "Sub-nyquist MIMO radar prototype with Doppler processing," in *Proc. IEEE Radar Conf.*, 2017, pp. 1179–1184.
- [42] S. Jokar and V. Mehrmann, "Sparse representation of solutions of Kronecker product systems," *Linear Algebr. Appl.*, vol. 431, no. 12, pp. 2437–2447, Dec. 2009.